INTERNATIONAL JOURNAL FOR NUMERICAL METHODS IN FLUIDS, VOL. 17, 501–541 (1993)

IS THE STEADY VISCOUS INCOMPRESSIBLE TWO-DIMENSIONAL FLOW OVER A BACKWARD-FACING STEP AT $Re = 800$ STABLE?

PHILIP M. GRESHO
Lawrence Livermore National Laboratory, University of California, P.O. Box 808, Livermore, CA 94551, U.S.A.
DAVID K. GARTLING AND J. R. TORCZYNSKI
Sandia National Laboratories, Albuquerque, New Mexico 87185, U.S.A.
K. A. CLIFFE AND K. H. WINTERS
AEA Technology, U.K.
T. J. GARRATT
Aspentec UK Ltd, Sheraton House, Castle Park, Cambridge, U.K.
A. SPENCE
School of Mathematical Sciences, University of Bath, U.K.
AND
JOHN W. GOODRICH
NASA Lewis Research Center, Cleveland, OH 44135, U.S.A.

SUMMARY

A detailed case study is made of one particular solution of the 2D incompressible Navier–Stokes equations. Careful mesh refinement studies were made using four different methods (and computer codes): (1) a high-order finite-element method solving the unsteady equations by time-marching; (2) a high-order finite-element method solving both the steady equations and the associated linear-stability problem; (3) a second-order finite difference method solving the unsteady equations in streamfunction form by time-marching; and (4) a spectral-element method solving the unsteady equations by time-marching. The unanimous conclusion is that the correct solution for flow over the backward-facing step at $Re = 800$ is steady—and it is stable, to both small and large perturbations.

KEY WORDS Backward-facing step Flow stability Incompressible flow

1. INTRODUCTION

The Second Minisymposium on Outflow Boundary Conditions was held at Stanford University in July 1991, at which four previously published benchmark (OBC's) solutions for the incompressible, Navier–Stokes equations were presented and discussed. A summary of this meeting is described in Gresho[1] and a more detailed description is in Sani and Gresho.[2] One of the benchmark problems was the two-dimensional flow over a backward-facing step (BFS) at a Reynolds number $Re = 800$. The benchmark solution for this case was published by Gartling[3]

0271–2091/93/180501–41$25.50

Received February 1993
Revised May 1993

and reported at the meeting. Eight other symposium participants, plus numerous previously published articles, obtained steady flow results that agreed—at least qualitatively—with this benchmark.

However, one notable presentation at the Stanford meeting disagreed markedly with the consensus result and stated emphatically that the flow at $Re=800$ was, in fact, not steady but rather time-dependent, with both eddies (top and bottom) oscillating about their alleged steady solution. The presenter of this opinion was A. Tomboulides with M. Israeli and G. Karniadakis as co-authors of the work. This new solution was produced using the 'exponentially-accurate-for-smooth-solutions' spectral element method.

Needless to say, the presentation did more than raise the eyebrows of the audience; the unqualified, matter-of-fact statements that all previous solutions were wrong also raised some ire and, of course, some serious concern. Could it be true that all others were wrong? The 'local' opinion at the meeting was 'perhaps, but not likely' since many previous studies (including six at the symposium) had, like Tomboulides *et al.*, used a time-marching approach to obtain, finally, a steady solution.

A primary concern, however, was that the benchmark problem statement and benchmark solution provided by Gartling[3] had *a priori* assumed the existence of a stable steady solution. This assumption was predicated on most previous results in the literature plus some pre-symposium (time-dependent) test calculations run at LLNL. The assumed steadiness of the flow allowed considerable computational economy as the stationary Navier–Stokes equations could be attacked directly on a series of increasingly refined meshes to demonstrate mesh convergence. No testing was done on solution stability for the benchmark report.

At the conclusion of the OBC minisymposium, Gartling was charged with the task of testing the steady flow result via the time-dependent equations. Additional simulations were to be run with some starting from 'rest' (actually potential flow, see Reference 4 for comments on impulsive starts), and others using various perturbations on the steady flow that were then followed in time. The results of these tests, which again indicated the correctness of the steady flow solution, were originally intended to be a small addition to the OBC minisymposium report by Sani and Gresho. The plan changed, however, with the subsequent appearance of an extensive article in *Journal of Fluid Mechanics* (JFM) by (basically) the same group from Princeton which focused on the backstep flow. The work of Kaiktsis *et al.*[5] (hereafter referred to as KKO) pronounced again that the flow does not possess a (stable) steady solution above $Re \cong 700$ and 'that the flow has undergone a second bifurcation at $Re=800$. The coexistence of two incommensurate frequencies at the relatively low Reynolds number $Re=800$ is, of course, consistent with the fact that this is a spatially developing flow exhibiting a very different spatial structure downstream.'

With the publication of the KKO result (and all the theory that was based on the result), we (Gartling, Gresho, and Sani) realized that a stronger, more focused response was required—and conceived the plan that finally resulted in this paper. It was our intention to determine the existence (or not) of a stable steady-state solution using four independent methods and four independent codes, all with sufficient refinement to preclude further debate. The computations were also performed *independently*; i.e. each code 'user' performed his portion before seeing what the others had done. The methods selected were:

(1) a time-marching finite element method,
(2) a steady (finite element) method that also *simultaneously* determines the stability (or not) of the solution,
(3) a time-marching finite difference method, and
(4) a time-marching spectral element method (almost identical to the method used by the Princeton group).

Because of the planned paper by Sani and Gresho for this journal, we selected this forum rather than JFM. We did announce to JFM readers (via a Letter to the Editor) that the paper in question contained some errors and referred them to this paper for details. Also, during the final stages of the preparation of this paper it became known by one of the authors (GK) that they had erred; we thus expect (and surely hope) that they will be sending their own 'errata' paper to JFM.

The remainder of this paper is as follows: after a few more remarks regarding the KKO paper, the new results—one set from each of the four codes mentioned above—will be presented. Finally, after some brief discussion of other supporting evidence, some appropriate conclusions and comments will be offered. We urge the reader to peruse the benchmark solution[2] for *details* regarding the steady solution; herein we merely summarize new results and how they were obtained.

Returning briefly to KKO, we wish to point out several items, with a partial view toward emphasizing how seemingly careful and well-done simulations can still give bad answers. All of our discussion is related to the 2D portion of their paper. (They also did many 3D simulations.)

It should be reported that the JFM simulations differed from those for the OBC test problem in two ways:

1. Their step filled only 47% of the channel vis-a-vis 50% for the test problem.
2. Their inflow boundary was located about one step height upstream of the expansion, whereas the test problem placed the inflow boundary at the same location as the expansion.

That these are unimportant differences derives from the following two facts:

1. They obtained the same type of result for the actual OBC test problem.
2. They stated in KKO that '... different upstream locations results in negligible differences in the flow field...'

In the Introduction, KKO refer to several recent numerical studies[6–8] but do not relate the fact that all except Sethian and Ghoniem[8] used conventional time-marching techniques and obtained *steady* solutions in the range of interest. Specifically, Osswald *et al.*[6] found steady solutions up to Re of at least 1474 (they found unsteady flow at $Re = 4000$), and Kim and Moin[7] found steady flow at $Re = 800$ (they went no higher). The vortex method of Sethian and Ghoniem, on the other hand, yielded unsteady results for Re as low as 250; however, they used a uniform velocity profile at the inlet, rather than a parabolic one, which significantly alters the solution.[9]

Regarding what appeared to be a serious attempt at grid refinement by KKO—a necessary condition for virtually all CFD simulations—we quote: 'Finally, experimentation with higher resolution per spectral element (using eleventh-order polynomial expansions instead of eighth) produced identical results for all simulations, indicating that the spatial resolution employed is sufficient for the range of Reynolds number considered here ($Re \leqslant 1300$). Regarding time accuracy, tests with schemes of order $J = 2$ and $J = 3$ (see Appendix) as well as time step $\Delta t = 10^{-2}$ and 10^{-3} resulted in differences of approximately 1%.' Thus, they did *try*, and this is certainly to their credit. But in the last of the four 'numerical' sections of this paper, we shall show that a harder try is necessary, at least using the spectral element method—and show how to do so.

For the record, we state below the problem whose (approximate) solution at $Re = 800$ is desired and, if the solution is steady, whose stability is to be investigated:

$$\frac{\partial \mathbf{u}}{\partial t} + \mathbf{u} \cdot \nabla \mathbf{u} = -\nabla P + Re^{-1} \nabla^2 \mathbf{u} \quad \text{and} \quad \nabla \cdot \mathbf{u} = 0, \tag{1}$$

where $Re \equiv \bar{u}H/\nu$ with $\bar{u}$ being the average inlet velocity and H the full channel height. The geometry for the computations is shown in Figure 1. The domain extends from the step face and

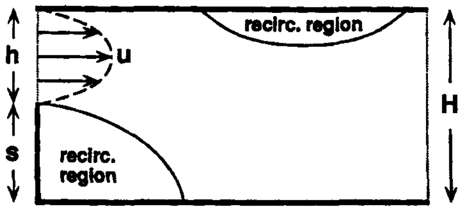

Figure 1. Backward-facing step geometry

inlet at $x=0$ to the outflow boundary, nominally at $x=15$ (30 step heights) although some simulations were performed with the outflow boundary at $x=17$ and $x=30$. The step and inlet are taken to have heights of $s=h=\frac{1}{2}$, and the channel walls are located at $y=\pm\frac{1}{2}$, providing a channel height of $H=1$. No-slip boundary conditions are applied on the channel walls and step face, and a parabolic velocity profile is applied at the inlet: $u_x=24\,y(\frac{1}{2}-y)$ and $u_y=0$. The OBC's were left to each analyst to choose since we are reasonably sure that they cannot be 'legislated' and very sure that the 'best' are not yet known—cf. the purpose of the OBC minisymposium.

2. NUMERICAL SIMULATIONS

This section contains summaries of the four independent studies conducted to answer the question posed in the title of this paper.

2.1. *A time-dependent finite element method*

As a first step in the investigation of time dependence in the BFS flow, a time-dependent finite element method was used to study the stability of the steady flow solution produced in Reference 3. For the results presented there, steady flows were obtained at $Re=800$ by use of a Newton iteration method coupled with zeroth-order continuation where solutions at $Re=200$, 400 and 600 were used as intermediate steps. In the present work three types of time-dependent simulations were studied which used the same software as described in Reference 3 and employed the same problem set-up and some of the same computational grids.

Run-up (time-marching) simulations. The most obvious approach for investigating the possibility of time-dependence in the backstep problem consists of simulating the $Re=800$ case as a time-accurate, transient problem starting from a quiescent initial condition. This approach mimics the general run-up technique employed by KKO, although the finite element method was used here in place of a spectral element method. The NACHOS II code (see Reference 10) was used to simulate this problem via an implicit, adaptive time step, predictor/corrector time-integration method. The predictor step employed an explicit, second-order Adams–Bashforth method; the implicit corrector utilized the second-order trapezoid rule. Since the predictor/corrector algorithm is not self-starting, the first two time steps are computed using the first-order backward Euler method and a small, fixed time step. A one-step Newton iteration was used in conjunction with the corrector step and the accuracy of the method was maintained through an adaptive time step procedure and a user-specified integration tolerance. The overall algorithm follows closely the widely used method described by Gresho *et al.*[11]

At time zero, the fully developed (parabolic) inlet velocity was imposed on the computational domain and the simulation allowed to run to steady state. The computation was terminated through a steady-state tolerance that required the L_2 norm of changes in the total velocity field between time steps to be less than 10^{-3}. A nominal integration tolerance of 0·001 was used for most simulations with select cases also run with a tolerance of 0·0005 to verify the temporal accuracy of the computations. The initial (non-dimensional) time step was set at $\Delta t=0{\cdot}01$, although the adaptive procedure increased this value by over three orders of magnitude by the end of the simulation. The computational mesh for the problem corresponded to mesh B (10 × 200 elements) in Reference 3 and extended to 60 step heights in the downstream direction. The mesh employed a 9-node, Lagrangian finite element approximation for the velocity components and a discontinuous linear pressure approximation. Grid convergence was again verified by rerunning the problem on mesh C (20 × 400 elements) as defined in Reference 3.

The transient response of the BFS run-up problem is composed of several stages. The initial velocity field is not divergence-free. However, the ill-posed, 'impulsive start' of this run-up simulation is converted to a well-posed initial value problem through use of the backward Euler method in the first time step; see Reference 4 for further details. At the end of the first step, the flow should be virtually potential with vortex sheets on the channel boundaries. Figure 2 shows contour plots of the stream function and vorticity for the first time step and the result is clearly as predicted—except for the vorticity at the inlet region which is generated by the specified (and non-'potential') boundary conditions. Velocity profiles taken across the channel at several streamwise stations show that the core flow is moving uniformly at the average velocity ($U_{\text{avg}}=0{\cdot}5$); the no-slip condition on the wall produces a thin region of high vorticity.

From the initial time step, the flow field evolves with a series of eddies (separation bubbles) being formed sequentially along the lower and upper walls. The development of the flow field is illustrated in a series of streamline plots in Figure 3. The first eddy forms at the step corner and

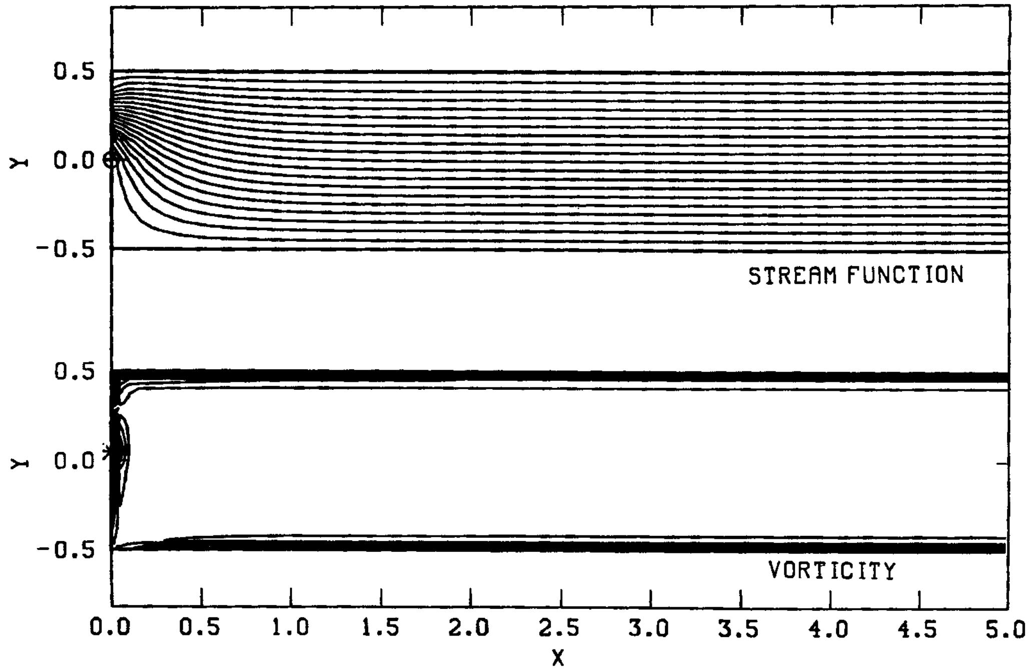

Figure 2. Streamines and vorticity contours for initial time step in run-up simulation

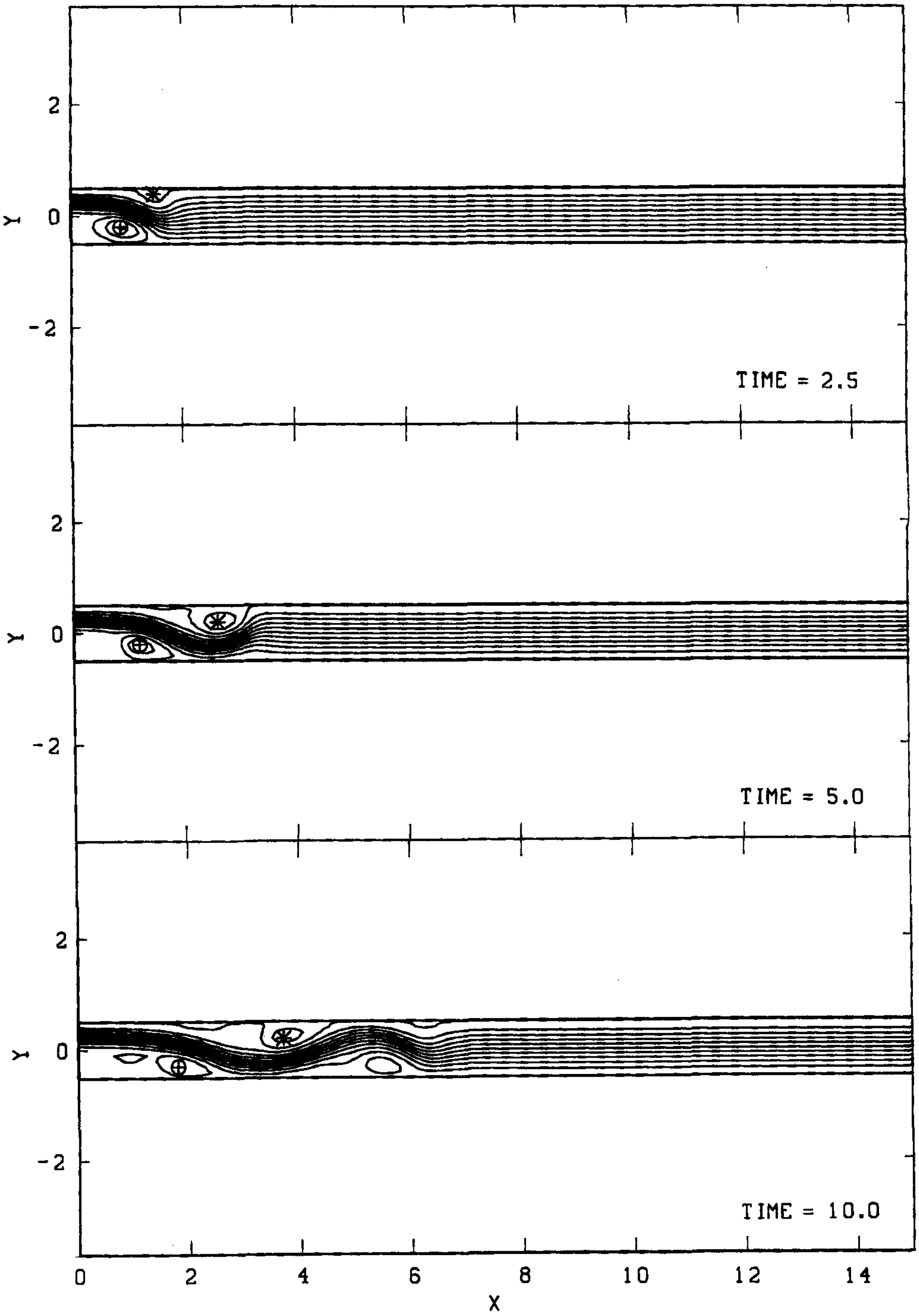

Figure 3. Streamlines during evolution of time-dependent simulation started from rest. Non-dimensional times $t=2{\cdot}5$, 5·0, 10·0, 15·0, 20·0 and 30·0

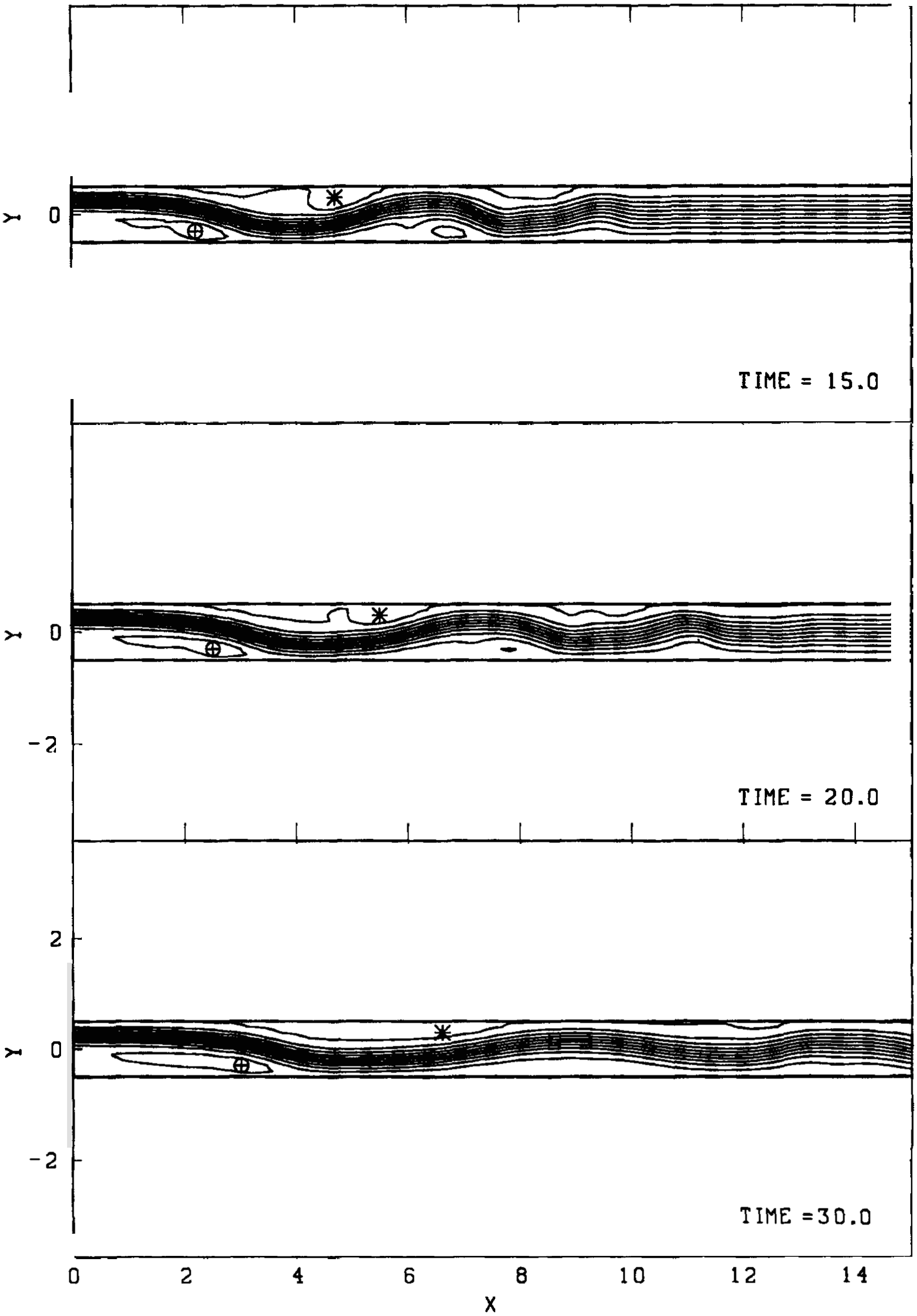

Figure 3. (Continued)

expands to form a separation region that is attached to the lower wall. As this primary eddy grows in the downstream direction, a second eddy forms and grows on the upper wall. Additional eddies of progressively smaller size are generated along the boundaries as the simulation proceeds. In concert with the staggered location and size of the wall separation zones, the main flow coming from the inlet is forced to follow a sinuous path along the channel. In the later stages of the flow development, the smaller (downstream) wall eddies are damped and disappear; the sinuous behaviour of the main channel flow decays and returns to a unidirectional flow that fills the channel cross-section. With the progressive elimination of each of the smaller eddies, the two major separation zones near the step undergo an adjustment in size and strength and slowly approach their steady-state configuration. No attempt is made here to explain the details and mechanisms involved in the temporal development of this flow as this would require significant further analysis. However, it should be noted that the transient eddy structures in this flow are relatively stationary in their spatial locations with their appearance/disappearance tied to the time-dependent meandering of the core flow. This is a marked distinction from the flow description in KKO, where eddies were described as being shed from the walls and convected out of the channel.

Despite the interesting features of this transient simulation, the essential question for this study is the long-term behaviour of the solution field. Figures 4 and 5 show the time history plots of the

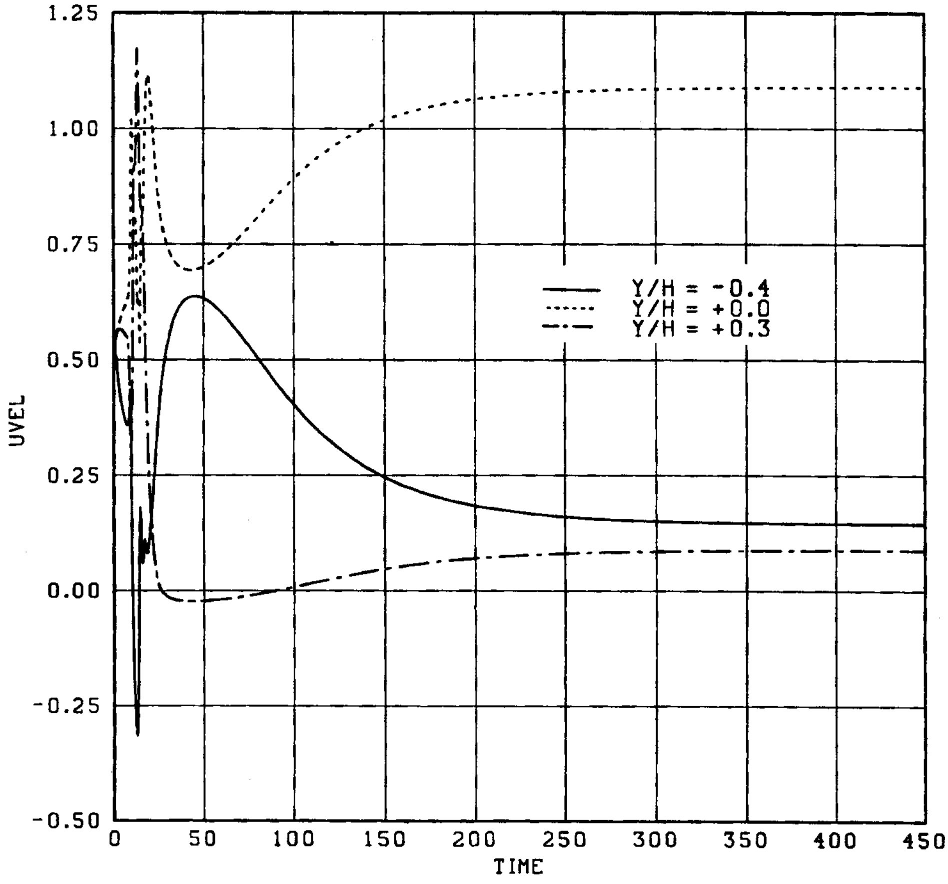

Figure 4. Time histories for the u velocity component at the $x/H=6$ station; time-dependent simulation started from rest

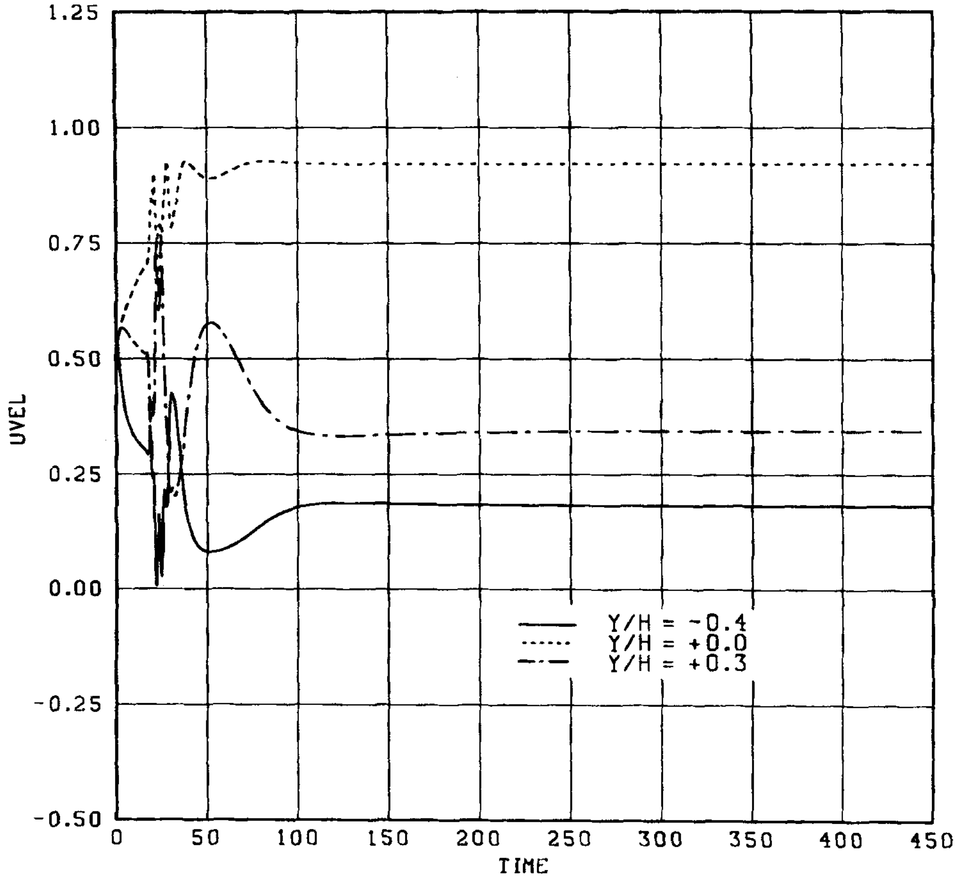

Figure 5. Time histories for the u velocity component at the $x/H=12$ station; time-dependent simulation started from rest

streamwise velocity component at several points across the channel for two stations located 12 ($x/H=6$) and 24 ($x/H=12$) step heights downstream of the corner. It is apparent from these figures and the previous description that the first 50–60 non-dimensional time units (approximately one transit period for the channel) are dominated by the formation and collapse of the distributed wall eddies. Figures 4 and 5 show a slow, monotonic decay to a time-invarant state with no evidence of the periodicity described in KKO. A comparison of the solution obtained at the end of the transient analysis with the steady results in Reference 3 showed virtually no difference in the solution fields.

Random perturbation simulations. A standard method of testing the local stability of a solution is to perturb it and observe the time-dependent response. If the perturbed solution returns to its steady-state value, the solution is deemed stable, while any other type of behaviour indicates a loss of stability. The steady backstep solution was tested using this technique. A random (positive or negative) perturbation to each component of the velocity field was generated for every nodal point in the grid. Four specific cases were tested in which the magnitude of the perturbation at each node was set at 1, 3, 10 or 20% of U_{max}. The perturbation field was added to the steady flow solution on mesh B and a time-dependent simulation was performed using the same integration algorithm as described previously. As before, the first backward Euler step projects the perturbations to the appropriate divergence-free subspace.

For each of the perturbation cases studied, the overall qualitative behaviour of the solution was the same, although the time required to return to a steady flow was slightly longer for the larger perturbations. Figures 6 and 7 show the time histories for velocity components at various points in the channel for the 10% perturbation case. The time-dependent response of this flow is very similar to the run-up case. The imposed perturbation field is sufficient to disturb the size and strength of the two major separation regions. This results in the development of a sinuous core flow with small wall eddies emerging on both walls. Eventually, the spatial oscillations in the core flow begin to diminish and the smaller eddies disappear; the perturbation field is damped in approximately one-half of the channel transit period (30 non-dimensional time units). Again, the asymptotic steady state produced by the time-integration process agreed with the original, unperturbed steady-state solution.

Periodic perturbation simulations. The final test of the stability of the steady flow solution was designed to perturb the flow at the frequency reported by Kaiktsis *et al.* From KKO, the

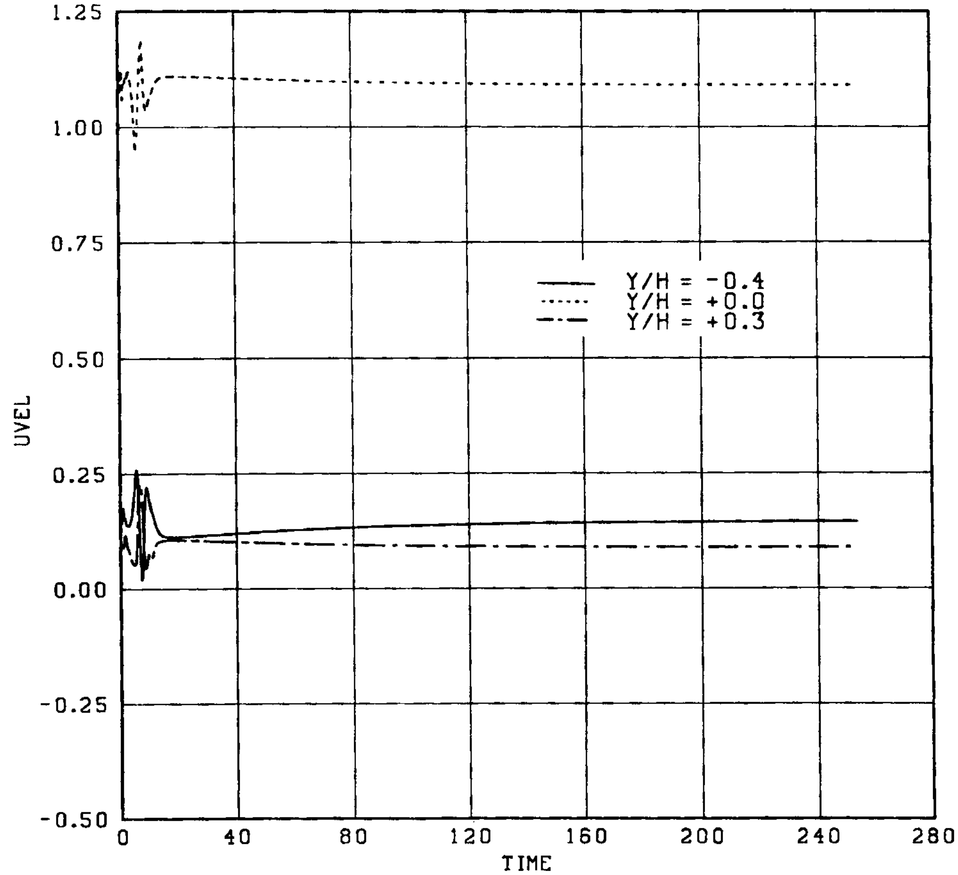

Figure 6. Time histories for the u velocity component at the $x/H=6$ station; time-dependent simulation started from a 10% random perturbation of the steady solution.

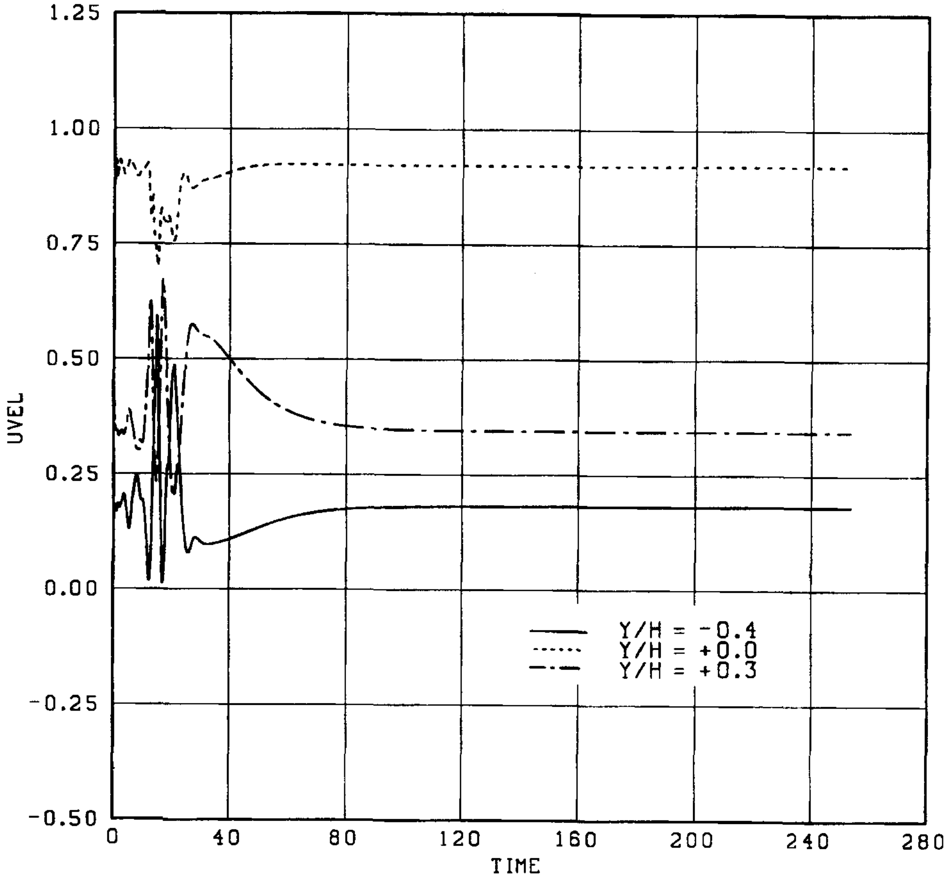

Figure 7. Time histories for the u velocity component at the $x/H = 12$ station; time-dependent simulation started from a 10% random perturbation of the steady solution

time-dependent flow at $Re = 800$ was reported to have a predominant frequency of 0·054. In an attempt to drive the steady flow unstable, the inlet velocity profile was modified to have a time periodic behaviour for three cycles, after which it was held at its original value. Two cases were studied, with the maximum amplitude of the oscillatory profile being 10 and 20% higher than the steady value at a frequency of 0·054. Solutions for this problem were generated on both meshes B and C.

During the time period that the inlet profile was varying sinusoidally, the channel flow responded with a series of time-dependent eddies along the upper and lower wall with a wavy streamline pattern in the core flow. Due to the pulsatile variation in the core flow, the two large separation zones close to the step were periodically subdivided into several smaller eddies and then recombined. When the inlet profile reverted to its steady value, the eddy structures began to decay and the flow slowly damped to its original steady state. Figures 8 and 9 provide time histories for the 10% perturbation case and Figure 10 shows the corresponding streamlines. Results for the 20% case were qualitatively similar. As in the previous two simulations, there was no evidence of a persistent time-dependent flow.

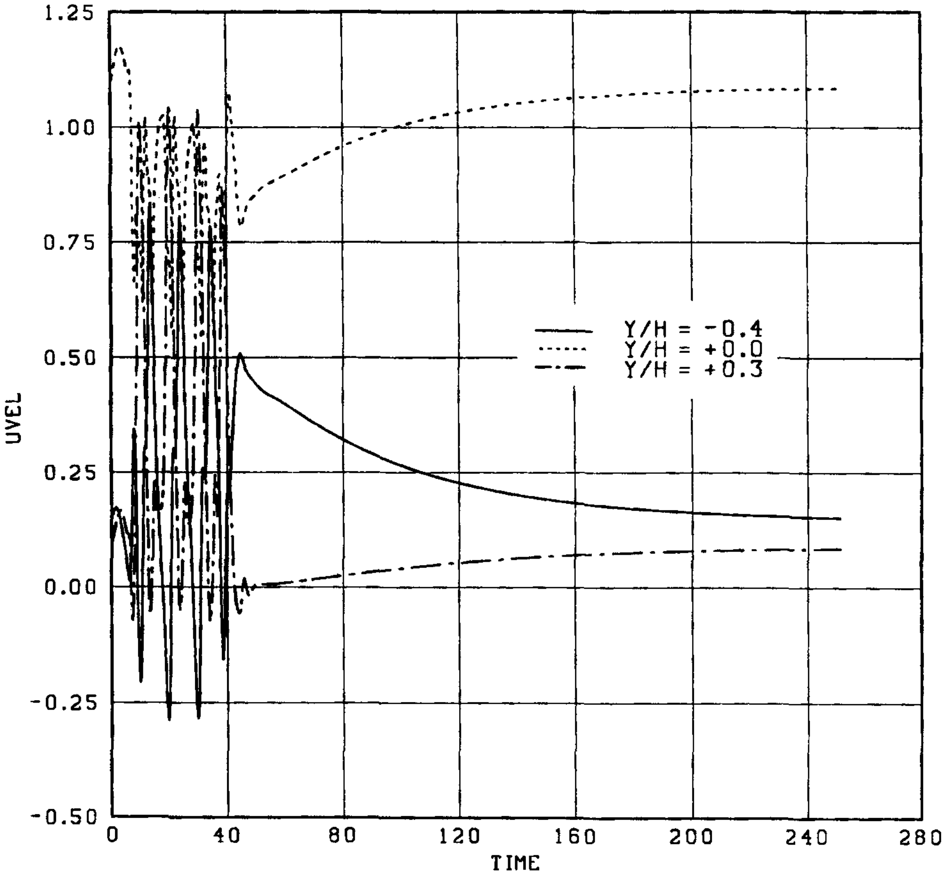

Figure 8. Time histories for the u velocity component at the $x/H=6$ station; time-dependent simulation started with a time-periodic inlet velocity

Conclusions. The simulations described here provide strong evidence that the claims made by KKO with regard to time dependence in the backstep problem are not correct. This conclusion will be corroborated by some of the results in subsequent sections. Of course, a *proof* that this flow is indeed time-independent can only be accomplished through a careful study of the bifurcation and stability problem. This topic is considered in the next section.

2.2. *A steady-state finite element stability analysis*

Using the finite element package ENTWIFE,[12] a mixed finite element approximation of (1) was obtained using nine-node quadrilateral elements with biquadratic interpolation for velocities and discontinuous piecewise-linear interpolation for pressures. (This is the same element pair used by Gartling, and is known to be one of the best 2D elements.[13]) This produces a finite-dimensional system of differential algebraic equations (DAE's) of the form

$$M\dot{u}+N(u, Re)u+Ku+CP=f, \quad C^{T}u=g, \tag{2}$$

where $f, u\in R^{n}$, and $g, p\in R^{m}$. Here $n>m$, M (mass matrix) and K (viscous matrix) are symmetric

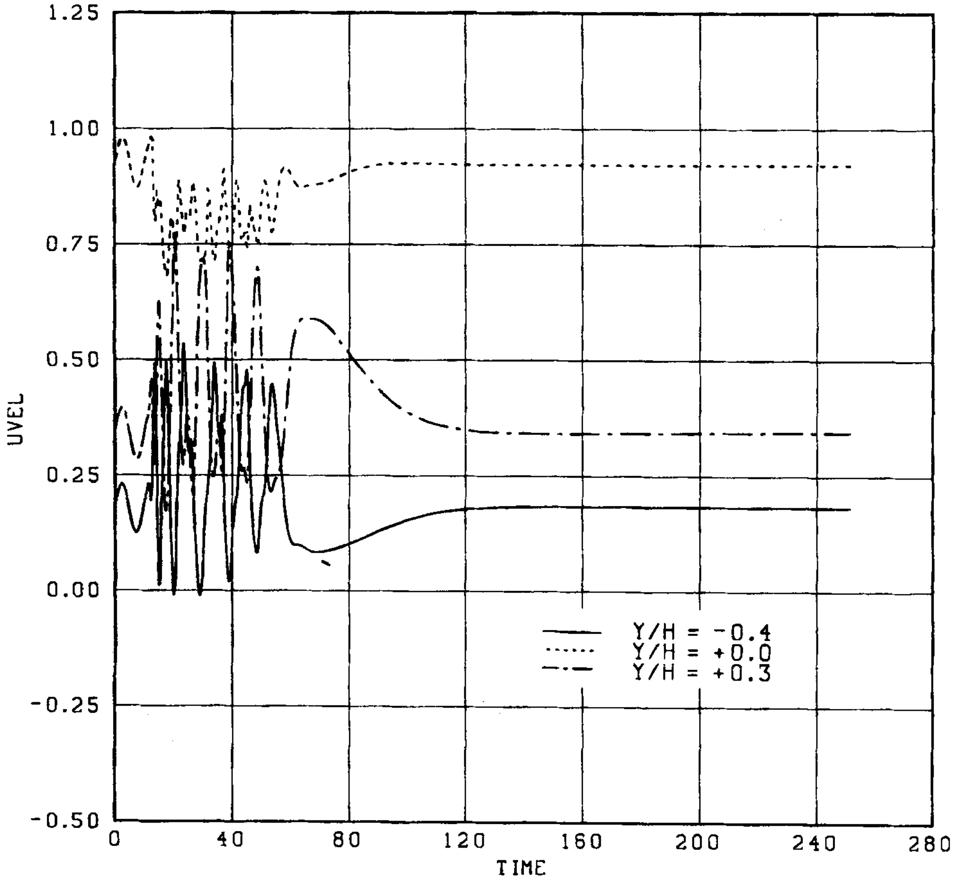

Figure 9. Time histories for the u velocity component at the $x/H=12$ station; time-dependent simulation started with a time-periodic inlet velocity

positive definite $n\times n$ matrices, $N(u, Re)$ is an $n\times n$ (advection) matrix and C is an $n\times m$ matrix of rank m. Also, u and P represent the components of the discretization of the velocity field and pressure, respectively. In block matrix form, (2) can be written as the time-singular ODE system—an index 2 DAE system (see Reference 13):

$$B\dot{v}+D(v, Re)v=h, \quad v, h\in R^N, \tag{3}$$

where

$$B=\begin{bmatrix} M & 0\\ 0 & 0\end{bmatrix}, \quad D(v, Re)=\begin{bmatrix} N(u, Re)+K & C\\ C^{\mathrm{T}} & 0\end{bmatrix}, \quad v=\begin{bmatrix} u\\ P\end{bmatrix}, \quad h=\begin{bmatrix} f\\ g\end{bmatrix}, \tag{4}$$

and $N=n+m$.

The simplest solutions of this system are the *steady-state solutions* (v, Re) which satisfy

$$D(v, Re)v=h; \tag{5}$$

and these may be computed for various Re values, for example, by numerical continuation techniques (e.g. Reference 14)—which we did. But we wish to determine in *addition* whether or not

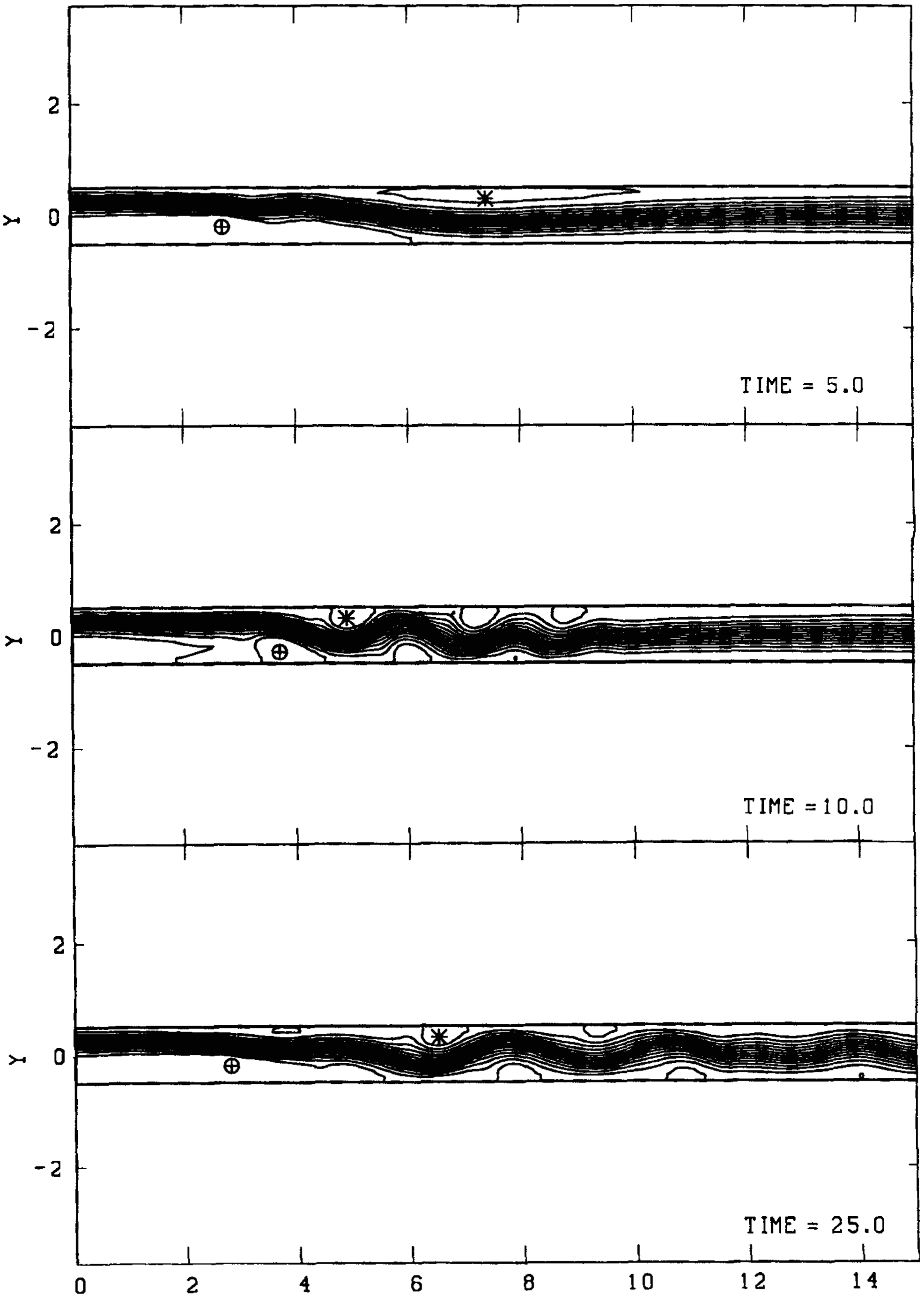

Figure 10. Streamlines during evolution of time-dependent simulation started with a time-periodic inlet velocity. Non-dimensional times $t = 5{\cdot}0$, 10·0, 25·0, 30·0, 45·0 and 50·0

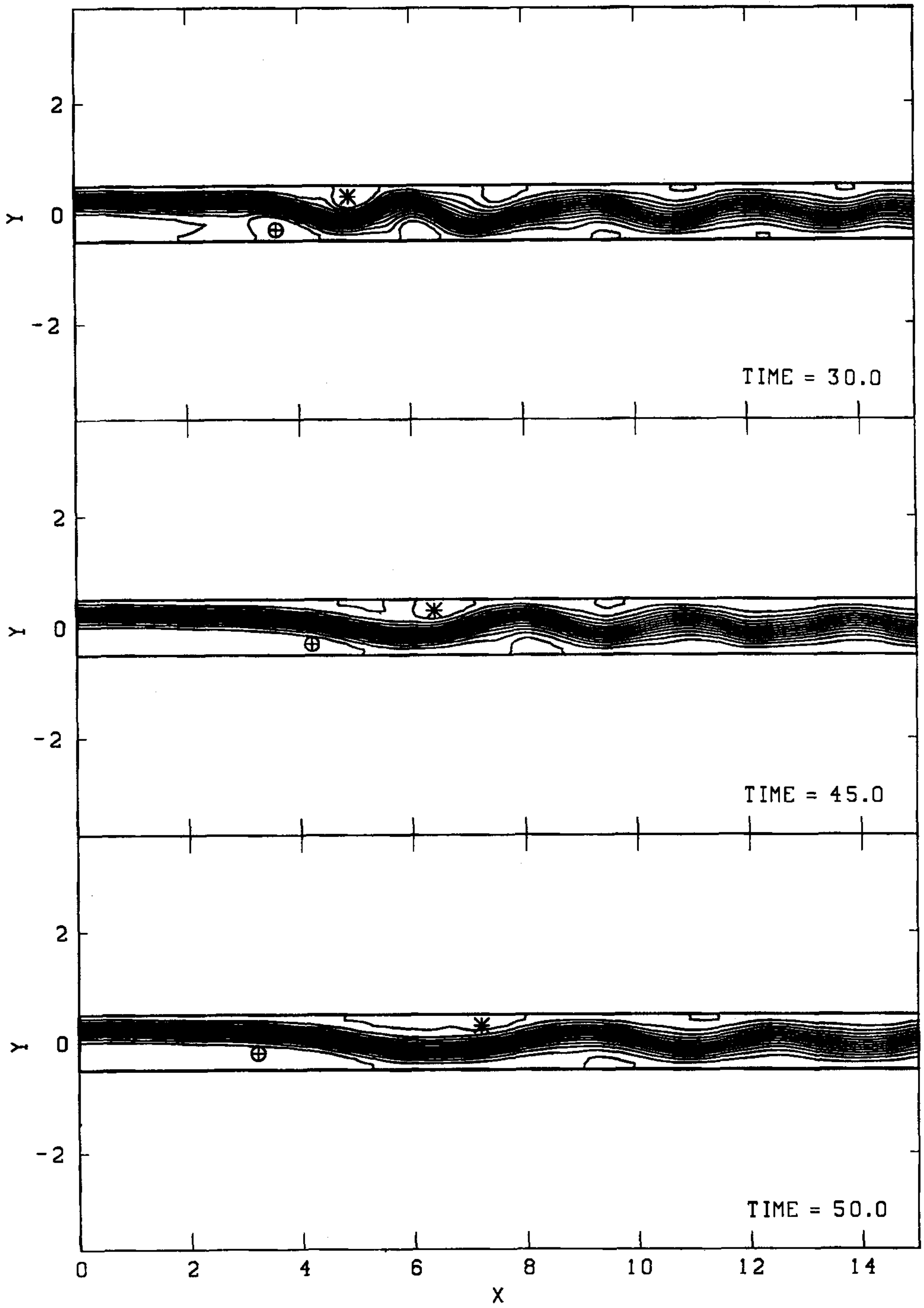

Figure 10. (Continued)

any steady-state solution attained is *stable* with respect to small disturbances, and this is discussed in the next subsection.

Eigenvalue calculations. To determine the stability of a steady-state solution (v, Re), the principle of linearized stability[15] requires that we linearize (3) about (v, Re) and analyse solutions of the perturbed homogeneous system

$$B\dot{w}+Aw=0, \quad w\in R^N, \tag{6}$$

where $A=D(v, Re)+D_v(v, Re)v$, $D_v\equiv\partial D/\partial v$ and A is called the Jacobian matrix. In fact, a steady-state solution of (2) is stable if and only if $\mathrm{Re}(\mu)>0$ for all eigenvalues μ of $A\hat{w}=\mu B\hat{w}$, where $w=\hat{w}e^{-\mu t}$. Hence, to determine stability we need to compute the eigenvalues of the generalized eigenvalue problem[16]

$$A\hat{w}=\mu B\hat{w}, \tag{7}$$

where A is an $N\times N$ matrix with the following block structure:

$$A=\begin{bmatrix} H & C \\ C^{\mathrm{T}} & 0 \end{bmatrix} \tag{8}$$

and $H=N(u, Re)+N_u(u, Re)u+K$ which is an $n\times n$ sparse non-symmetric matrix. If the eigenvalues $\{\mu_i\}$ of (7) are ordered by increasing real part (i.e. $i<j\Rightarrow\mathrm{Re}(\mu_i)\leqslant\mathrm{Re}(\mu_j)$), then to determine stability it is sufficient to compute μ_1 and declare a steady-state solution of (2) (and thus, hopefully, of (1)) stable (unstable) if $\mathrm{Re}(\mu_1)>0$ $(\mathrm{Re}(\mu_1)<0)$.

The basic idea behind finding the most dangerous eigenvalue of (7) is to transform the problem into one in which the most dangerous eigenvalue corresponds to an extremal eigenvalue which can be found by a standard iterative scheme. We have used a modified Cayley transform to achieve this. The transformed eigenvalue problem was solved using the subspace iteration method which is guaranteed to find the extremal eigenvalue if the starting subspace is not defective in the corresponding eigenvector. There are a number of technical difficulties associated with the fact that (7) is a *generalized* eigenvalue problem with B being structurally singular. A complete discussion of the implementation of the algorithm and the resolution of the technical difficulties can be found in Reference 17. Further details regarding the eigenstructure of (7) for $Re=0$ (Stokes equations) can be found in Reference 18, wherein it is shown that this eigenproblem is defective: there are only $n-m$ finite and positive eigenvalues with corresponding (discretely) divergence-free eigenvectors; the remaining $2m$ modes have infinite eigenvalues which are equally split between m eigenvectors (in the pressure only) and m generalized (and not discretely divergence-free) eigenvectors (in the velocity only), each of the former serving to generate one of the latter. For $Re>0$, the basic structure remains the same with the exception that, because of the unsymmetric matrix, the eigenvalues can be complex and it is no longer certain that the $n-m$ divergence-free modes have $\mathrm{Re}(\mu_i)>0$.

Results. In our finite element discretization we used a mesh (which gave results) virtually identical to that (those) of Gartling,[3] i.e. a uniform distribution of elements across the channel, a uniform distribution in the upstream region of $0\leqslant x\leqslant 15$ and a smoothly graded distribution in the flow direction for the region $15\leqslant x\leqslant 30$, so that elements near $x=30$ were approximately twice the length of the elements near $x=15$.

All computations were performed using a Cray 2 supercomputer in single (64 bit) precision on the same meshes (A–D) as used by Gartling.[3]

We now turn our attention to the question of the stability of the computed steady-state solutions. A tolerance of $\varepsilon=10^{-5}$ (Reference 17) was set for computation of an approximation $\tilde{\mu}_1$,

Table I. Computed most dangerous eigenvalue for meshes A and B for various *Re*

Re	Mesh A		Mesh B	
	MV	$\tilde{\mu}_1$	MV	$\tilde{\mu}_1$
200	171	38·39741	241	38·89636
400	241	20·09698	241	21·24205
600	241	15·39194	241	15·05634
800	241	16·58417	241	14·94673

Table II. Computed most dangerous eigenvalue for meshes A–D for $Re=800$

Mesh	MV	$\tilde{\mu}_1$
A	241	16·58417
B	241	14·94673
C	241	15·06843
D	241	15·06489

say, to the most dangerous eigenvalue μ_1. We computed $\tilde{\mu}_1$ for mesh A for $Re=200, 400, 600, 800$ with a subspace of size $k=10$ in the subspace iteration method.[19] We also computed $\tilde{\mu}_1$ for mesh B for the same values of *Re*. The results are given in Table I, where the number of matrix–vector multiplies (MV) for each problem is also shown. (The computation is dominated by the matrix–vector multiplications so that MV is a measure of the computational performance of the method.)

Following the advice given in Reference 17, various values of k—the size of the subspace in the subspace iteration method—were used to ensure that convergence is consistent and we thus also computed $\tilde{\mu}_1$ at $Re=800$ for (mesh A) for $k=20$, 30 and 40. Convergence to 16·58417 was observed for all the values. As a final check, we computed $\tilde{\mu}_1$ for mesh A for $Re=800$ but using 100 orthogonal iterations in the verification step to increase the possibility of an approximation to an eigenvalue to the left of 16·58417 appearing. It turned out that one did not and we thus conclude that the steady-state solution for $Re=800$ on mesh A is *stable*.

Finally, we computed $\tilde{\mu}_1$ at $Re=800$ for meshes A–D for $k=10$ with the results given in Table II. The computations at these finer meshes indicate that the most dangerous eigenvalue is near to 15.

Conclusions. We have applied new iterative techniques for computing the most dangerous eigenvalue of the linearized Navier–Stokes equations to the problem of flow over a backward-facing step at a Reynolds number of 800 and an expansion ratio of 2·0. The results indicate that this flow is stable.

Careful checks have been carried out to ensure that the most dangerous eigenvalue has indeed been found. The only way to be absolutely sure is, of course, to compute *all* the eigenvalues; however, this is not a practicable proposition for such large problems. The technique we have used, namely subspace iteration on an appropriately transformed problem, is almost certain to find the most dangerous eigenvalue. Being based on the power method, it can only fail if the initial approximation to the subspace has virtually no component of the most dangerous eigenvalue—which is not very probable. As an additional check, a verification step was carried out in which 100 additional iterations were performed for one particular case (mesh A, $Re=800$).

The calculations were also carried out on a range of grids and showed little sensitivity to grid refinement. Thus, we are reasonably confident that we have found the most dangerous eigenvalue for the flow over a backward-facing step at $Re=800$ and, since this eigenvalue is definitely positive, the flow is stable.

2.3. A time-dependent finite difference method

Summary description of the numerical method. The velocity field for two-dimensional incompressible flows can be written in terms of the stream function ψ as $u(\mathbf{x}, \mathbf{t})=\partial\psi/\partial y$ and $v(\mathbf{x}, \mathbf{t})=-\partial\psi/\partial x$. Equation (1) thus becomes

$$\frac{\partial^2\psi}{\partial t}+\frac{\partial\psi}{\partial y}\nabla^2\frac{\partial\psi}{\partial x}-\frac{\partial\psi}{\partial x}\nabla^2\frac{\partial\psi}{\partial y}-\frac{1}{Re}\nabla^4\psi=0 \quad \text{for } \mathbf{x} \text{ in } \Omega, \text{ and } t>0. \tag{9}$$

The data for the problem in this formulation consists of the initial values for ψ and boundary data, such as the standard set of boundary conditions $\psi(\mathbf{x}, t)=\beta(\mathbf{x}, t)$ and $\partial\psi/\partial n(\mathbf{x}, t)=\gamma(\mathbf{x}, t)$ for $\mathbf{x}$ in $\partial\Omega$, and $t>0$ where $\partial\Omega$ is the boundary of Ω, and $\partial/\partial n$ is differentiation in the exterior normal direction at the boundary. A steady-state form of (9) was previously used by Schreiber and Keller[20] with path continuation methods for calculating steady high Reynolds number cavity flows.

We use a centred spatial differencing for (9), a Crank–Nicolson (trapezoid rule) time differencing for the diffusion terms, and a second-order Adams–Bashforth time differencing for the convection terms—and a fixed Δt. The velocity components are directly recovered from the discrete stream function by central differencing, with all three variables being defined at each grid point. The velocity solution is exactly (discretely) divergence-free with respect to a central difference formulation of the divergence operator.

The artificial outflow boundary condition that we use is

$$\frac{\partial^2\psi}{\partial x^2}=0 \quad \text{and} \quad \frac{\partial^2\omega}{\partial x^2}=0, \tag{10}$$

where $\omega\equiv\nabla^2\psi$, via second order backward-difference formulas for the derivatives.

The Crank–Nicolson differencing scheme for the diffusion term in (9) does not impose a stability constraint on the time step size, while the Adams–Bashforth differencing scheme for the convection terms does impose a stability constraint. We have successfully used $0{\cdot}15\leqslant\|u\|\,\Delta t/\Delta x\leqslant 0{\cdot}85$, for Reynolds numbers in the range $100\leqslant Re\leqslant 25\,000$, with grid sizes in the range $1/384\leqslant\Delta x=\Delta y\leqslant 1/16$. The truncation error for this method is $O(\Delta t^2)+O(\Delta x^2)$.

The implicit operator in the discrete time-stepping equation combines the Laplace and biharmonic operators, and a multigrid method is used to solve this equation at each time step. The approach that we have used is an adaptation of a method for biharmonic problems that was developed by Linden.[21] The essential detail is that the biharmonic operator is factored as two Laplacians. The multigrid solver for the resulting system of two second-order elliptic equations uses point Gauss–Seidel relaxation as the smoothing operator, with linear restriction and prolongation. A simple V-cycle iteration scheme is used, with 3 iterations at each grid level while coarsening, and with no iterations while refining. At each time step, 10 to 20 V-cycles are used to reduce the residuals to less than $5{\cdot}0\times10^{-11}$ or $5{\cdot}0\times10^{-12}$, depending upon the problem. The factoring of the biharmonic operator as two Laplacians introduces the vorticity $\omega = \nabla^2\psi$ *only* for the purpose of having a convergent iteration scheme, but it incidentally produces both ψ and ω as the simultaneous solution of coupled Poisson and Laplace equations. Note that there are no boundary conditions (except at outflow) applied to the vorticity—in agreement with the conclusions of Gresho.[22]

The algorithm is extremely robust with respect to Reynolds number, and has been used to compute directly transient incompressible flows with smoothly resolved stream function, kinetic energy and vorticity contours for Reynolds numbers as high as $Re = 25\,000$. The standard steady state for the lid-driven cavity is obtained at $Re = 7500$ with $\Delta x = 1/256$, but the algorithm does produce unsteady time-asymptotic states in the lid-driven cavity for $Re = 10\,000$ with $\Delta x = 1/128$ and $\Delta x = 1/192$. These results suggest that $Re = 800$ is well within the range of Reynolds number where the algorithm will neither generate purely numerical instabilities, nor unduly dampen any instability that is inherent in the dynamics of the Navier–Stokes equations. Further details are given in References 23–27.

Numerical results. The inlet boundary conditions are those of Gartling;[3] for initial conditions we simply continued the boundary data at $x = 0$ down the entire channel length. The resulting initial condition is an artificial state with a constant parabolic flow profile in the upper half of the channel for its entire length, with no flow in the lower half of the channel. This can perhaps be thought of as the initial data for a popped membrane problem with a horizontal membrane separating two different steady-flow states. Three different simulations have been conducted for this problem, with three different grids. A coarse grid simulation has been run with $\Delta x = \Delta y = 1/32$ and $\Delta t = 1/80$, a medium resolution simulation with $\Delta x = \Delta y = 1/64$ and $\Delta t = 1/200$ and a fine grid simulation with $\Delta x = \Delta y = 1/128$ and $\Delta t = 1/800$. All three simulations were run out to the non-dimensional time $t = 400$ and in all cases the channel length is 15 (30 step heights).

The initial transient evolution of the medium resolution simulation is presented in Figure 11 as a sequence of stream function contour plots for $t = 5$, 10, 15, 20, 25 and 30. In Figure 11(a) at $t = 5$, the lower and upper eddies are already present, although both eddies are very far upstream from their final positions. In Figure 11(b) at $t = 10$, a very significant wavy disturbance has developed in the flow field downstream from these eddies. In Figure 11(c) at $t = 15$, there is a small distinct third recirculation on the lower wall. In Figure 11(d) at $t = 20$, there are additional small distinct eddies on both the upper and lower walls. In Figure 11(e) at $t = 25$, the upper and lower eddies are both single large recirculations, and the small recirculations on the upper and lower walls have disappeared, leaving only slight waves in the flow field as the last indication of their presence. In Figure 11(f) at $t = 30$, the upper and lower eddies are both in the form that will persist, although they are both slowly creeping down the walls and stretching, and there is a slight waviness in the downstream flow field still visible from the effect of the initial transient. The flow at $t = 400$ for the 960×64 grid is displayed in Figure 12. Figure 12(a) gives the stream function contours, showing the two eddies stretched and shifted downstream from their locations at $t = 30$ in Figure 11(f). The vorticity and kinetic energy contours at $t = 400$ are displayed in Figure 12(b) and 12(c). The transient dynamics displayed above show that the nearly 'steady-state' results that have been obtained at $t = 400$ with the time-dependent finite difference simulation do not depend upon initial data that are chosen either to be near the desired steady state, or to avoid vigorous dynamics that might initiate a flow instability that could lead to an unsteady state.

The portrayal of the transient evolution given above is purely qualitative, and is entirely inadequate for making a compelling case that the time-asymptotic state is indeed a steady flow. Several variables have been recorded at each time step in order to monitor more carefully the time evoluton of these simulations. The change in the solution during a single time step is monitored

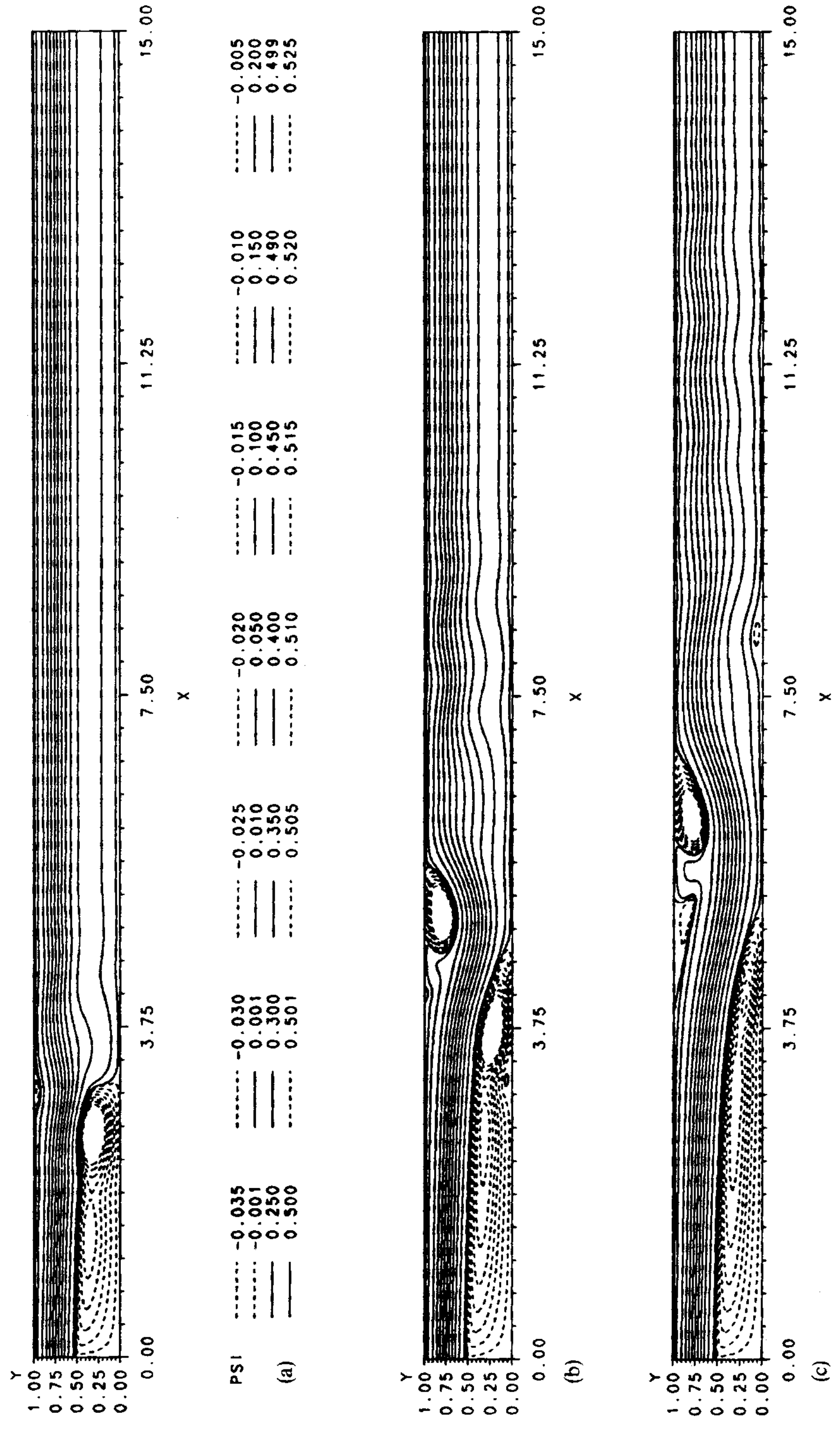

Figure 11. Stream function contour plots, 960 × 64 grid: (a) $t = 5$; (b) $t = 10$; (c) $t = 15$; (d) $t = 20$; (e) $t = 25$; (f) $t = 30$

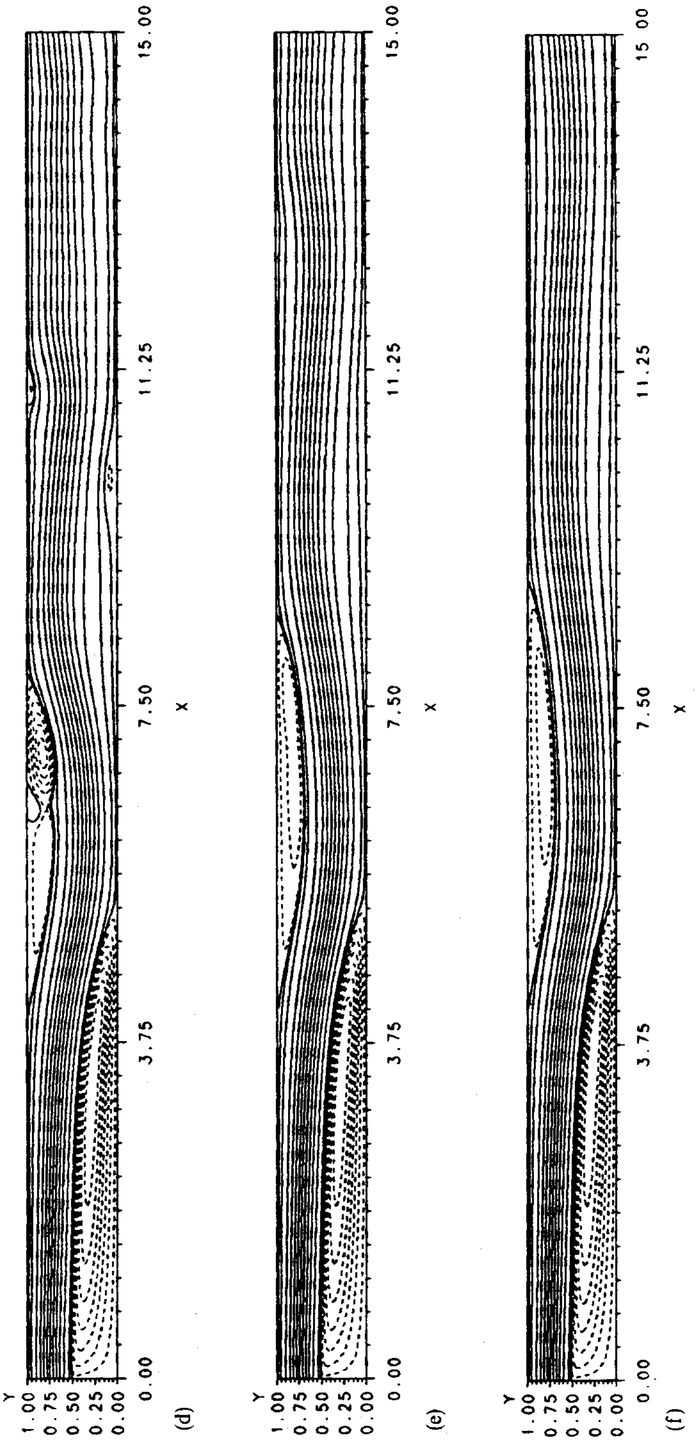

Figure 11. (Continued)

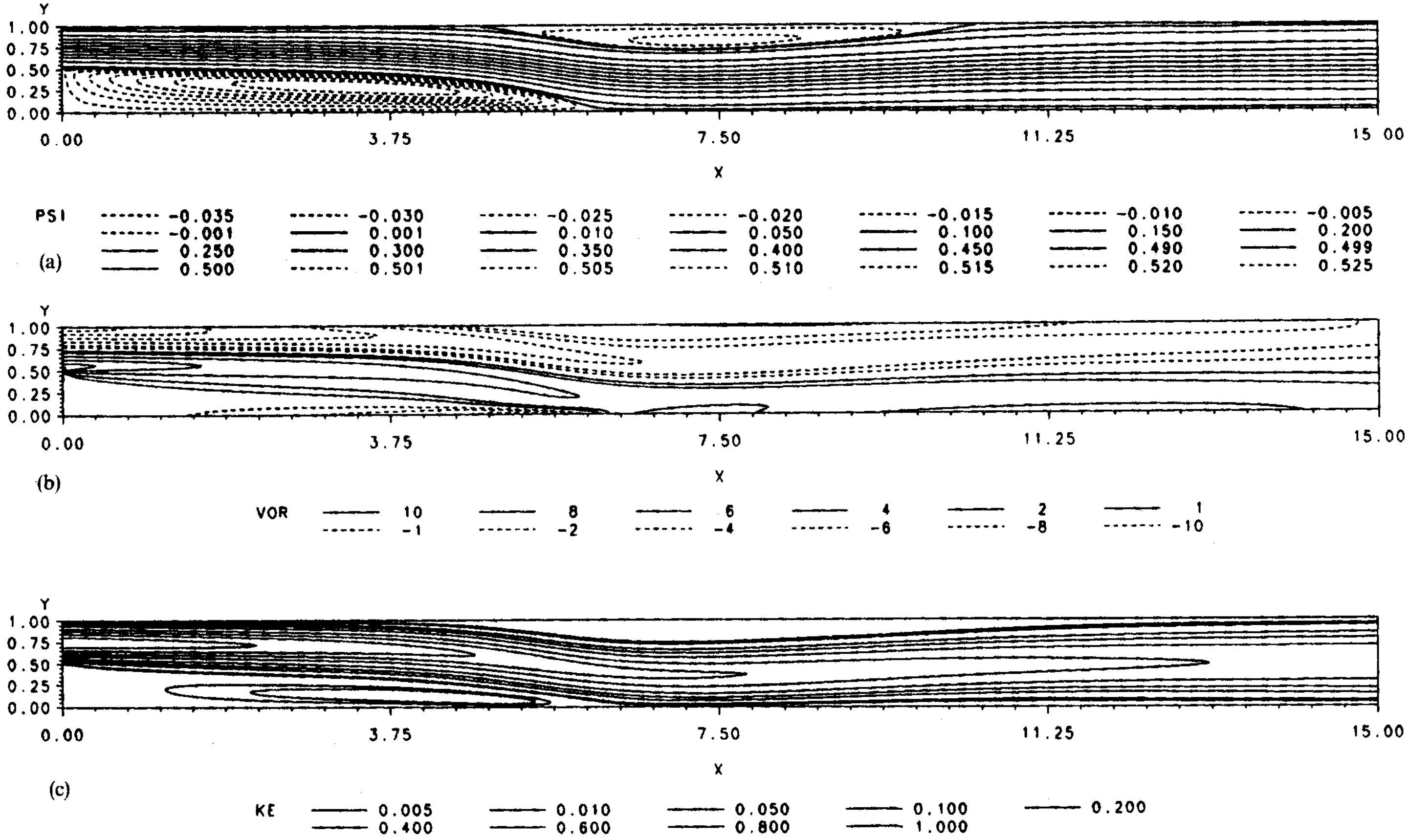

Figure 12. The final state at $t = 400$, 960×64 grid: (a) stream function contours; (b) vorticity contours; (c) kinetic energy contours

by the relative L_1 norm of the stream function change per time step, defined as

$$\frac{\sum_{i,j} |\psi_{i,j}^{n+1} - \psi_{i,j}^{n}|}{\sum_{i,j} |\psi_{i,j}^{n+1}|}$$

and the relative L_1 norm of the vector field change per time step, defined as

$$\frac{\sum_{i,j} (|u_{i,j}^{n+1} - u_{i,j}^{n}| + |v_{i,j}^{n+1} - v_{i,j}^{n}|)}{\sum_{i,j} (|u_{i,j}^{n+1}| + |v_{i,j}^{n+1}|)}.$$

The qualitative state of the flow is monitored by the global stream function maximum in the middle of the upper eddy, and the global stream function minimum in the middle of the lower eddy. Note that the centre of the upper and lower eddies is always taken to be on a grid point. The qualitative state of the flow is also monitored by the total kinetic energy of the entire flow, defined as

$$\frac{1}{2} \Delta x \Delta y \sum_{i,j} (u_{i,j}^{n+1})^2 + (v_{i,j}^{n+1})^2.$$

Figure 13(a)–(e) presents the five variables monitoring the evolution of the flow simulation on the 960 × 64 grid for $100 \leqslant t \leqslant 400$. The stream function change per time step in Figure 13(a), and the velocity field change per time step in Figure 13(b), are both $O(10^{-7})$ by $t \approx 200$. These two indicators are similar to measures that are used to monitor convergence to a steady state, and $O(10^{-7})$ is below the levels that are commonly used to stop a time evolution with a declaration that a steady state has been attained. Note in Figure 13(e) that the change in the total kinetic energy for $100 \leqslant t \leqslant 400$ is occurring in the 5th and 6th significant digits. All of the data in Figure 13 show a gradually slowing monotonic approach to a time-asymptotic value, certainly for $t > \sim 130$. There is a complete absence of any amplifying or oscillatory behaviour.

Table III presents stream function values and grid point co-ordinates for the stream function extrema that occur at the centres of the upper and lower eddies of the 1920 × 128 fine grid

Table III. Stream function values at eddy centres 1920 × 128 grid

t	Stream function	x	y	Stream function	x	y
100	−0·034196	3·351	0·2890	0·507791	7·1406	0·7968
120	−0·034181	3·390	0·2890	0·507464	7·2500	0·8046
140	−0·034174	3·421	0·2890	0·507213	7·2968	0·8046
160	−0·034179	3·343	0·2968	0·507029	7·3671	0·8125
180	−0·034184	3·359	0·2968	0·506904	7·3906	0·8125
200	−0·034187	3·359	0·2968	0·506814	7·3984	0·8125
220	−0·034190	3·3671	0·2968	0·506750	7·4140	0·8125
250	−0·034192	3·375	0·2968	0·506688	7·4218	0·8125
300	−0·034194	3·375	0·2968	0·50663	7·4296	0·8125
350	−0·034194	3·375	0·2968	0·506617	7·4296	0·8125
400	−0·034195	3·375	0·2968	0·506609	7·4375	0·8125
Ga	−0·0342	3·350	0·300	0·5064	7·400	0·800

Note: The row labelled Ga is the steady reference solution (see Reference 3)

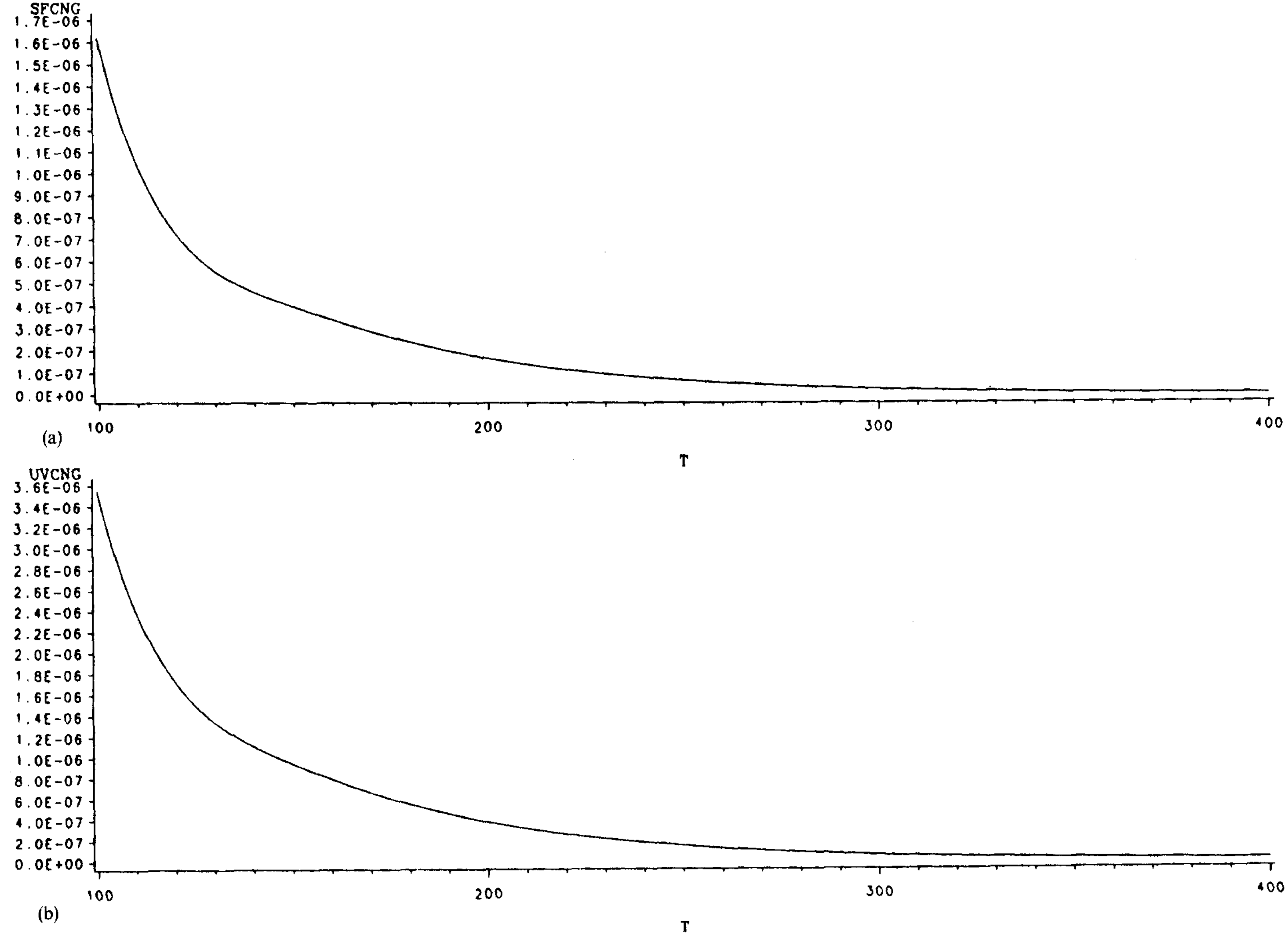

Figure 13. Scalar diagnostic variables for $100 \leqslant t \leqslant 400$, 960×64 grid: (a) relative L_1 norm of the stream function change per time step; (b) relative L_1 norm of the velocity field change per time step; (c) global stream function maximum; (d) global stream function minimum; (e) total kinetic energy

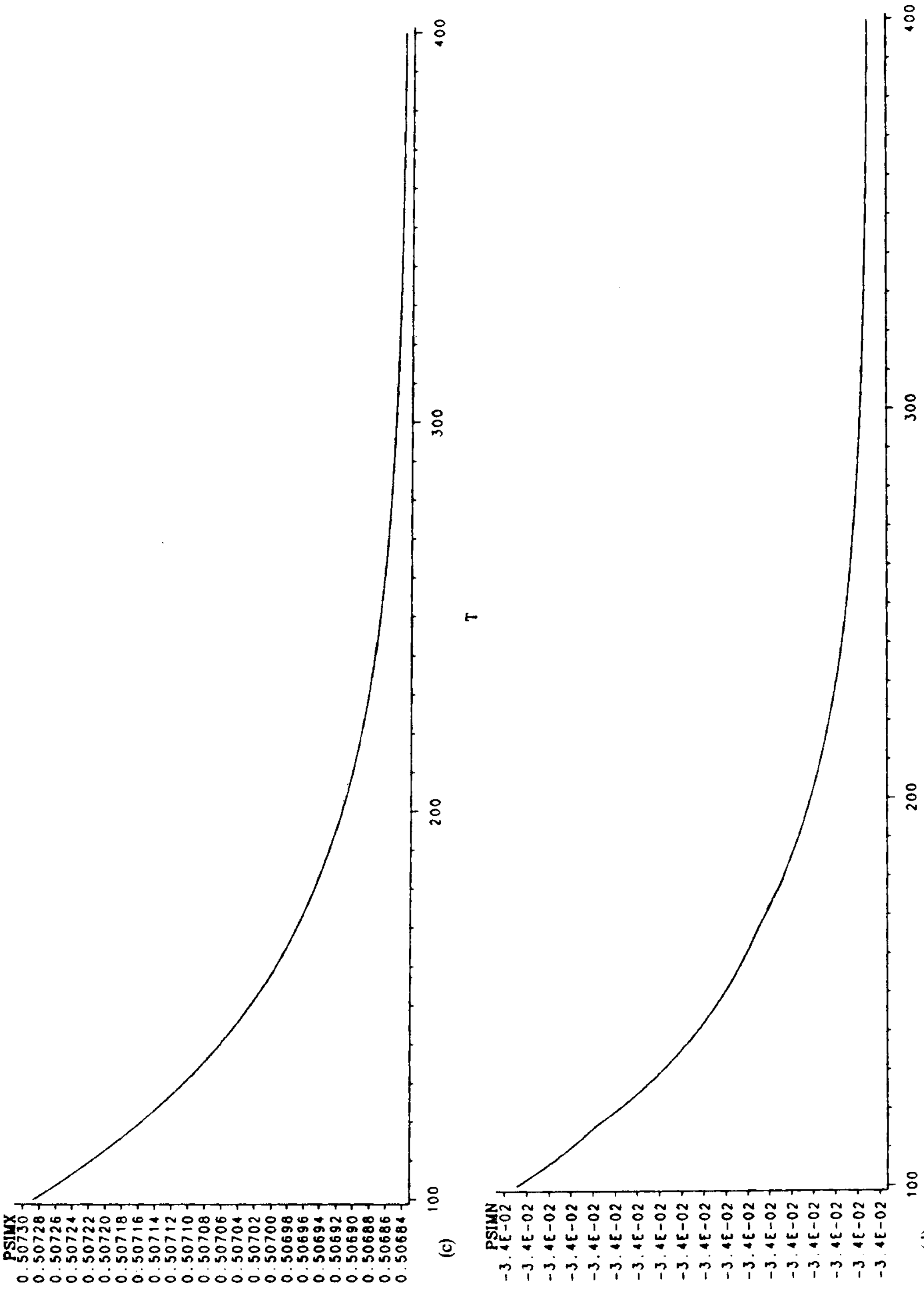

Figure 13. (Continued)

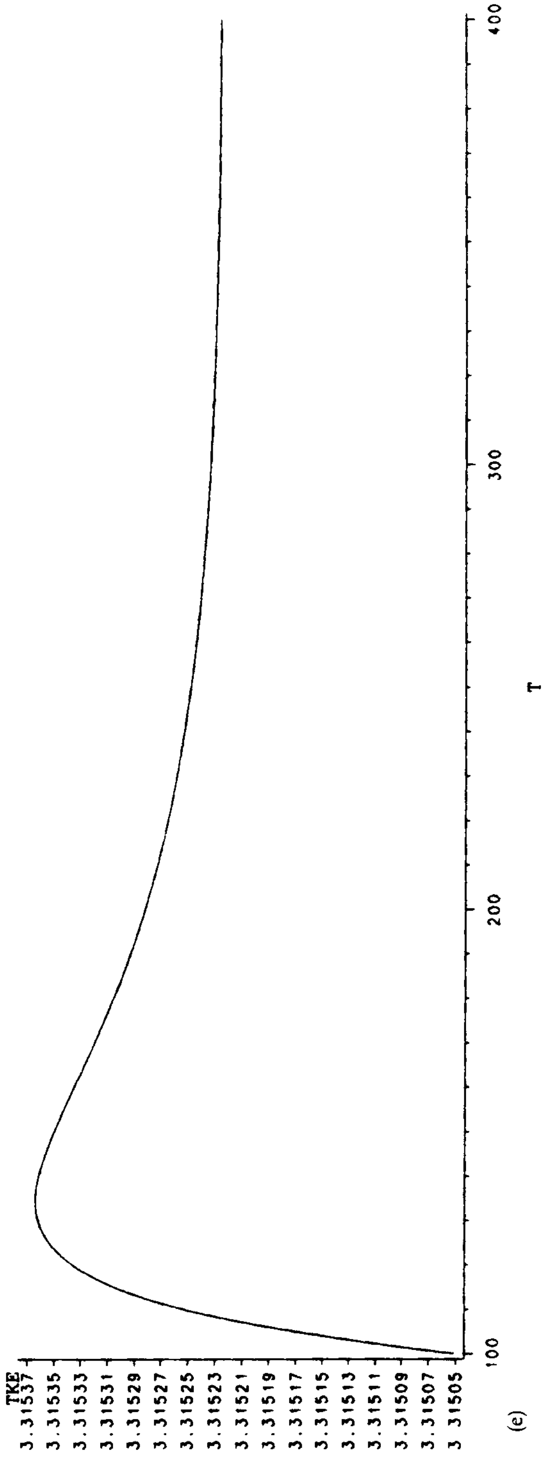

Figure 13. (Continued)

simulation. Note that the time intervals between successive rows of data are 20 non-dimensional time units for the first seven rows, and either 30 or 50 non-dimensional time units for the last four rows. The global stream function minimum data are presented in the left half of Table III. Note that the stream function minimum in the lower eddy gets larger (closer to 0) until $t \approx 140$, and then the stream function minimum becomes monotonically smaller (further from 0) up to $t=400$. Note also that the x co-ordinate for the centre of the lower stream function eddy has a local in time maximum at $t \approx 140$, then a local in time minimum at $t \approx 160$, with a progressively slower monotonic increase toward a time asymptotic value as $t \rightarrow 400$. Note in particular that for $250 \leqslant t$, the co-ordinates for the centre of the lower eddy do not change, and the minimum stream function value at the eddy centre changes monotonically in the 5th significant digit. The global stream function maximum data are presented in the right half of Table III. The stream function maximum in the upper eddy decays monotonically from a maximum attained before $t=100$, with change in the 5th significant digit for $250 \leqslant t$. Note that the x co-ordinate change from $t=200$ to $t=220$ is 2/128, or two grid points, while the change from $t=220$ to $t=250$ is one grid point, the change from $t=250$ to $t=300$ is one grid point, and the change from $t=300$ to $t=400$ is one grid point. This clearly shows a gradual but slowing monotonic change toward a time-independent value.

The evolutions of the stream function maximum and minimum from the fine grid simulation are plotted in Figure 14 for $380 \leqslant t \leqslant 400$. These plots clearly show in detail the non-oscillatory gradually slowing monotonic change in the final stages of the fine grid evolution for the stream function extrema. Over this time interval the stream function maximum changes from 0·506611635 at $t=380$ to 0·506609304 at $t=400$, and the stream function minimum changes from $-0{\cdot}0341949929$ at $t=380$ to $-0{\cdot}0341950703$ at $t=400$. The cumulative changes over these 20 non-dimensional time units for the stream function maximum and minimum are $-2{\cdot}33 \times 10^{-6}$ and $-7{\cdot}74 \times 10^{-8}$, respectively. This change is over 16000 time steps, and by any reasonable measure can be considered to be gradual. Note that both plots are showing a decrease in the stream function extrema, but that the stream function maximum is coming closer to 0, while the stream function minimum is going further from 0. This behaviour is consistent with the medium resolution simulation, and indicates a weakening of the upper eddy and a strengthening of the lower eddy.

Table IV presents separation and reattachment points, and eddy lengths, for the upper and lower eddies from the 1920 × 128 fine grid simulation. The data in Table IV are presented for the same time values as the data in Table III. The separation and reattachment points are defined as points on the boundary where the vorticity $\omega=0$. These x values are obtained by linear interpolation between two grid points where the vorticity changes sign. The eddy length for the upper eddy is defined as the difference between the x co-ordinates of its separation and reattachment points. The lower eddy length is defined as the x co-ordinate of its reattachment point. The lower eddy shows a monotonic lengthening that is consistent with the medium resolution simulation and indicates a strengthening of the lower eddy. For $h=\Delta x=\Delta y=1/128$, the approximate change in lower eddy length from $t=200$ to $t=220$ is $3{\cdot}07\,h$, from $t=220$ to $t=250$ is $2{\cdot}90\,h$, from $t=250$ to $t=300$ is $2{\cdot}34\,h$, from $t=300$ to $t=350$ is $0{\cdot}91\,h$ and from $t=350$ to $t=400$ is $0{\cdot}36\,h$. The upper eddy shows a monotonic shortening, which is consistent with the monotonic decay of the stream function maximum at the centre of the upper eddy, and is another indication of the gradual weakening of the upper eddy. The upper eddy separation point is monotonically increasing, but its reattachment point shows a local in time maximum at $t \approx 120$, with monotonic decrease for $120 \leqslant t$. The approximate change in upper eddy length from $t=200$ to $t=220$ is $-3{\cdot}50\,h$, from $t=220$ to $t=250$ is $-3{\cdot}32\,h$, from $t=250$ to $t=300$ is $-2{\cdot}68\,h$, from $t=300$ to $t=350$ is $-1{\cdot}04\,h$ and from $t=350$ to $t=400$ is $-0{\cdot}41\,h$. Both the lower and upper eddy

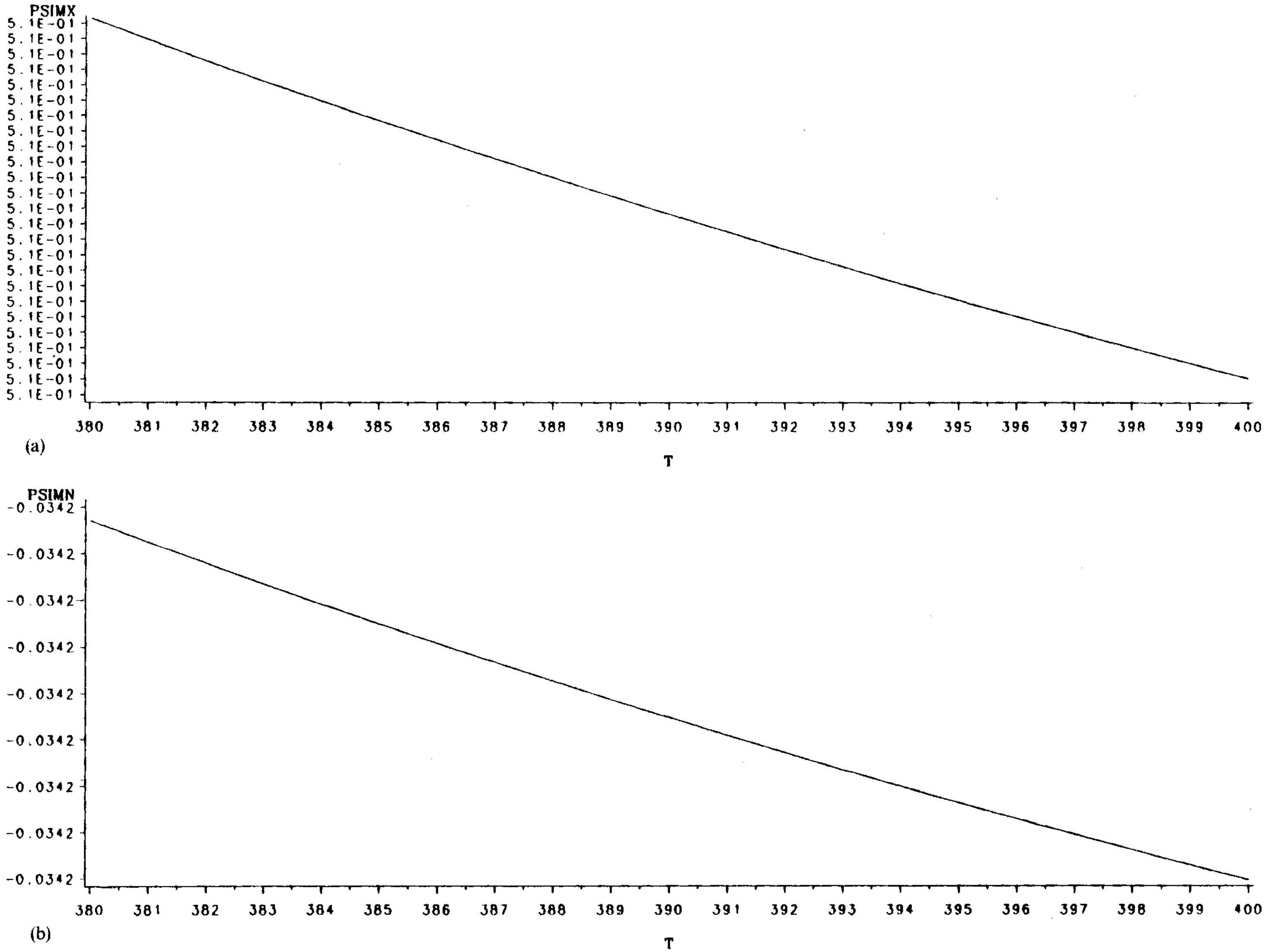

Figure 14. Stream function extrema for $380 \leqslant t \leqslant 400$, 1920×128 grid: (a) stream function maximum at the centre of the upper eddy, $0{\cdot}5066093 \leqslant \psi_{\max} \leqslant 0{\cdot}5066116$; (b) stream function minimum at the centre of the lower eddy, $-0{\cdot}03419507 \leqslant \psi_{\max} \leqslant -0{\cdot}03419499$

Table IV. Eddy lengths, 1920 × 128 grid

t	Lower eddy length	Upper eddy start	Upper eddy stop	Upper eddy length
100	5·5761	4·3710	10·5059	6·13483
120	5·7369	4·5193	10·5215	6·00216
140	5·8462	4·6204	10·5105	5·89009
160	5·9208	4·6895	10·4979	5·80838
180	5·9718	4·7368	10·4880	5·75114
200	6·0068	4·7693	10·4809	5·71157
220	6·0309	4·7916	10·4758	5·68419
250	6·0535	4·8126	10·4709	5·65825
300	6·0718	4·8296	10·4669	5·63730
350	6·0789	4·8362	10·4654	5·62917
400	6·0817	4·8388	10·4648	5·62597
Ga	6·10	4·85	10·48	5·63

Note: The row labelled Ga is the steady reference solution (see Reference 3)

length data clearly show the gradually slowing monotonic change that is typical of convergence to a steady state.

Figure 15 presents the relative L_1 norm of the stream function and velocity field changes per time step from the 1920 × 128 fine grid simulation for $380 \leqslant t \leqslant 400$. Note that the scale of change for both indicators is $O(10^{-9})$ for the entire interval $380 \leqslant t \leqslant 400$. The total kinetic energy for this simulation shows the same behaviour, monotonically changing from 3·32051176 at $t=380$ to 3·32050964 at $t=400$, to the precision that these data are stored. The time evolution of this recorded data is represented as 212 discrete single digit step decreases of $-1{\cdot}0 \times 10^{-8}$ in the total kinetic energy over 16 000 time steps, and cannot be plotted by the graphics package that is being used. Since the changes in the flow eddies are all monotonic, even the very gradual evolution that this simulation shows for $t \approx 400$ can still accumulate to a noticeable change when integrated over a long time interval, so the eddy characteristics estimated by this flow at $t=400$ must be accepted with appropriate caution.

Conclusions. The problem of always approaching but never reaching the steady time asymptotic state is generic to the use of time-dependent codes for calculating 'steady-state' results. It can even occasionally happen that a very weak instability gradually becomes amplified over a very long time period until a noticeable unsteady time-asymptotic state is clearly manifested. This type of behaviour in the square-driven cavity occurs near the critical Reynolds number for a Hopf bifurcation to a periodic unsteady time-asymptotic state, and is associated with small secondary and tertiary recirculations in the cavity corners. The instabilities are actually present for $Re \approx 5000$, but they are damped out in the time evolution until $Re \approx 8900$.[24, 26] The crucial point is that oscillatory behaviour is observed at Reynolds numbers below the critical Reynolds number for a Hopf bifurcation, but the oscillations are damped (by definition) for subcritical Reynolds numbers. This type of damped oscillation is entirely missing from the simulation data for the BFS which suggests that $Re=800$ is clearly below the critical Reynolds number for a Hopf bifurcation to a periodic time-asymptotic flow. The gradually slowing non-oscillatory monotonic change displayed by all of the data for this simulation is completely consistent with and strongly supportive of the conclusion that the flow over the backward-facing step is steady at $Re=800$.

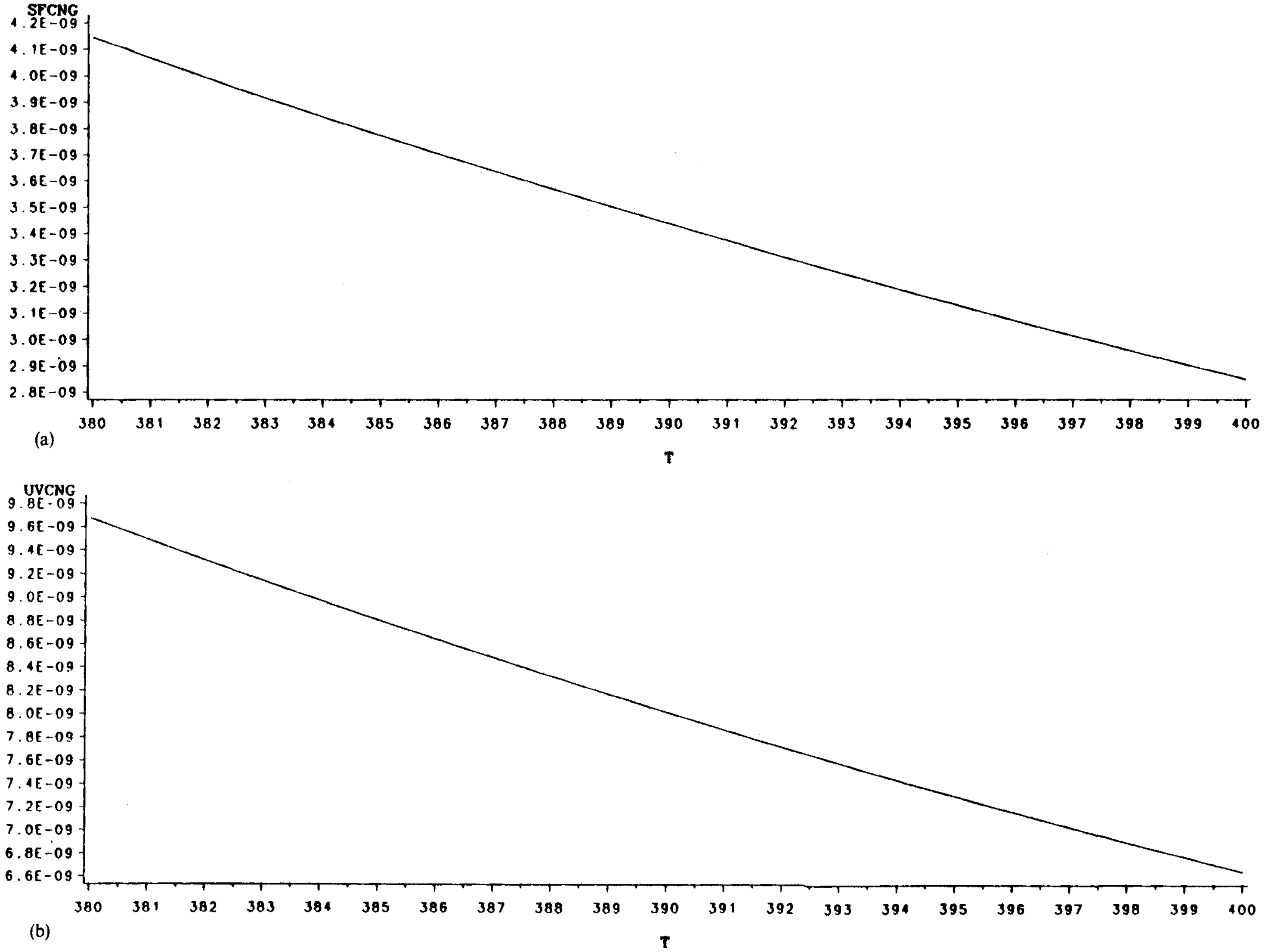

Figure 15. Convergence measures for $380 \leqslant t \leqslant 400$, 1920×128 grid: (a) the relative L_1 norm of the stream function change per time step; (b) the relative L_1 norm of the velocity field change per time step

2.4. *A time-dependent spectral element method*

In this section, a time-dependent spectral element method is applied to simulate the two-dimensional transient flow of an incompressible fluid over a backward-facing step at a Reynolds number of $Re=800$. The geometry employed in these simulations is as discussed in the previous sections. The corner of the step is taken to be the origin of the co-ordinate system, and the downstream channel extends a distance $L/H=17$ downstream from the step. This channel length is chosen to be equivalent to that of KKO and is in harmony with the study of Gartling,[3] which indicates that channels with lengths $L/H \geqslant 15$ are sufficiently long to preclude undue influence of the finite channel length on the flow at $Re=800$. The following conditions are applied on the boundaries of the computational domain: $u=v=0$ on the horizontal walls, $-p+\mu \partial u/\partial n=0$ and $\partial v/\partial n=0$ on the outflow boundary, and $u=[\tanh(t/4)]u_B(y)+[1-\tanh(t/4)]u_P(y)$ and $v=0$ on the inflow boundary and the step face. Here $u_B(y)=\max[0, 24y(\frac{1}{2}-y)]$ is the correct inlet boundary condition and $u_P(y)=3(\frac{1}{2}-y)(\frac{1}{2}+y)$ is the Poiseuille flow observed infinitely far downstream whenever steady flow is asymptotically obtained. With this inflow boundary condition, fluid actually flows *through* the step at early times (see Figure 16); however, the boundary condition is virtually identical to $u_B(y)$ for times $t \geqslant 30$. Note too that this boundary condition maintains a time-independent mass flux through the inflow boundary. The initial velocity field is set equal to $u=u_P(y)$ and $v=0$ everywhere in the domain. Thus, the above combination of boundary and initial conditions allows the simulations to be initialized using an exact divergence-free solution of the Navier–Stokes equations, namely Poiseuille flow. Furthermore, since the

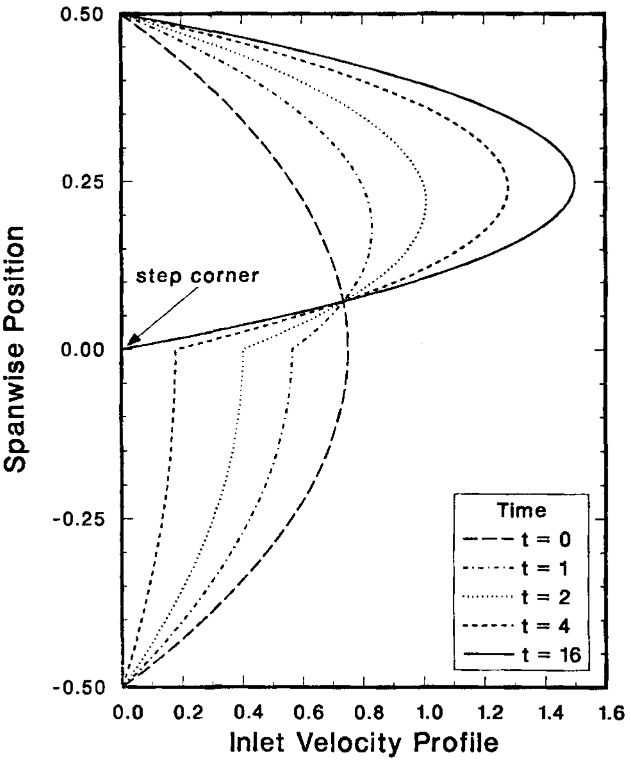

Figure 16. The inflow velocity profile at selected times. Note that at early times flow actually passes through the step surface

inflow boundary condition is varied smoothly in time from Poiseuille flow to flow over a backward-facing step, the flow experiences an order-unity transient that is probably strong enough to excite sustained unsteady behaviour, if that is the appropriate long-time behaviour for the simulation.

All simulations discussed in this section are performed with the computational fluid dynamics code NEKTON v2.8.[28] NEKTON employs an Uzawa spectral element method similar to that developed by Patera.[29] In brief, the spectral element method is a high-order finite element method: each element has N^D velocity nodes and $(N-2)^D$ pressure nodes, where D is the dimensionality. The velocity nodes are located at Gauss–Lobatto collocation points, some of which are on the element boundaries, whereas the pressure nodes are located at Gauss points, none of which are on the element boundaries. The velocity components and the pressure are represented within an element by sums of D-dimensional tensor products of $(N-1)$- and $(N-3)$-order Lagrangian-interpolant polynomials, respectively, based on velocity and pressure nodal values. Thus, from one element to an adjacent one, the velocity components are continuous, whereas the pressure is discontinuous. Henceforth, the quantity N will be referred to as the element order, even though it is not strictly the order of the polynomials used to represent the fields. To avoid solving a non-linear non-symmetric system of equations at each time, NEKTON advances the convective term $\mathbf{u}\cdot\nabla\mathbf{u}$ explicitly in time, but all other terms are treated implicitly. This explicit feature imposes a Courant restriction on the size of the maximum time step.

There are two methods available in NEKTON to examine the effects of mesh refinement on a numerical solution. First, as in conventional finite element (and finite difference) methods, the computational domain can be subdivided ever more finely into progressively smaller elements. Second, unlike most finite element methods, the element order N can be increased without modifying the original subdivision of the computational domain. In this latter case, it is believed that 'spectral convergence' will result:[28, 29] errors decrease exponentially in the number of nodes, rather than algebraically, as would result from fixing the element order and further subdividing the domain. Both of these methods for determining whether solutions are mesh-independent are examined below.

Simulations. Three grids of differing resolution, denoted L (low), M (medium) and H (high), are employed in the simulations (see Figure 17). In this section, the term 'grid' is used to denote the subdivision of the computational domain into spectral elements, without regard to the element order, whereas the term 'mesh' is used to denote the actual nodes resulting from a specified element order N and a specified spectral element grid. The H grid with element order $N=7$ yields a mesh that is comparable in nodal density to the C mesh of Gartling,[3] on which the *steady* solution is found to be adequately resolved. Similarly, the L grid is comparable to the KKO grid,

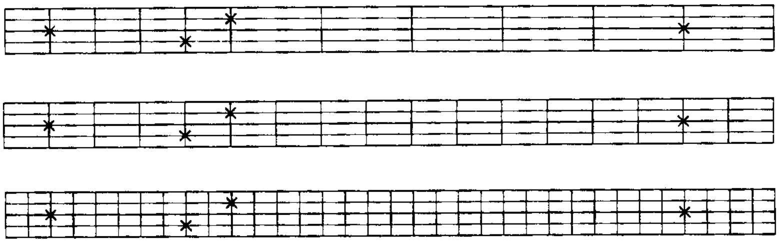

Figure 17. The three NEKTON grids: top, L grid; middle, M grid; bottom, H grid. Velocity and pressure histories are recorded at points (1, 0), (4, −0·25), (5, 0·25) and (15, 0), indicated by crosses (×)

Table V. Mesh refinement results

Case	Grid	Order N	Temporal behaviour
L09	L	9	Numerical errors
L10	L	10	Numerical errors
L11	L	11	Unsteady chaotic
L12	L	12	Steady oscillatory
M07	M	7	Numerical errors
M08	M	8	Steady oscillatory
M09	M	9	Steady oscillatory
M10	M	9	Steady monotonic
H05	H	5	Numerical errors
H06	H	6	Numerical errors
H07	H	7	Steady monotonic
H08	H	8	Steady monotonic
H09	H	9	Steady monotonic

with which an element order of $N=9$ was used. At this element order, the resultant mesh has a nodal density in the streamwise direction that is only about 40% of the Gartling C mesh and thus may have only marginal resolution for steady flow at $Re=800$, based on the results of Gartling.[3] The maximum element aspect ratios (streamwise length to spanwise length) are 8:1, 4:1, 2:1 and 4:1 for the L grid, the M grid, the H grid, and the Gartling C mesh, respectively.

Table V shows a categorization of the simulations performed for $Re=800$ based on the grid and the element order that are employed. In each simulation, a fixed time step of $\Delta t=0{\cdot}025$ is employed. This value is chosen so that the Courant limitation imposed by the explicit treatment of the convective term is satisfied even for the cases with the highest spatial resolution. Although the time-integration scheme in NEKTON is capable of adapting the time step, this option is not employed here. Each simulation is advanced to a time of $t=200$, which appears to be long enough to determine the asymptotic temporal behaviour of the flow, indicated in Table V by brief qualitative descriptions.

Four general classes of behaviour are observed for the numerical solutions. First, 'steady monotonic' denotes evolution toward an asymptotically steady state by means of a monotonic decay of the transient after the starting transient has been convected out of the computational domain. Second, 'steady oscillatory' denotes evolution toward an asymptotically steady state by means of a decaying, or damped, oscillation. Third, 'unsteady chaotic' denotes sustained irregular transient behaviour with no indication of evolution toward steady behaviour. Fourth, 'numerical errors' denotes termination of a numerical solution by a floating-point exception. This results from the velocity field becoming non-physically large within one element. Velocity histories exhibiting steady monotonic and unsteady chaotic behaviours are shown in Figure 18, and the corresponding streamlines are shown in Figure 19. Cases H08 and H09 yield nearly identical spatial and temporal variations of pressure and velocity and thus are believed to represent mesh-independent solutions. Additionally, the locations of the separation and reattachment points of the recirculating regions, shown in Table VI, are in good agreement with the results of Gartling.[3]

Discussion. A clear trend emerges from these results. When the resolution is increased beyond a certain point, the numerical solution evolves toward an asymptotically steady flow by a monotonic decay of the transient. However, as the resolution is decreased, the numerical solution

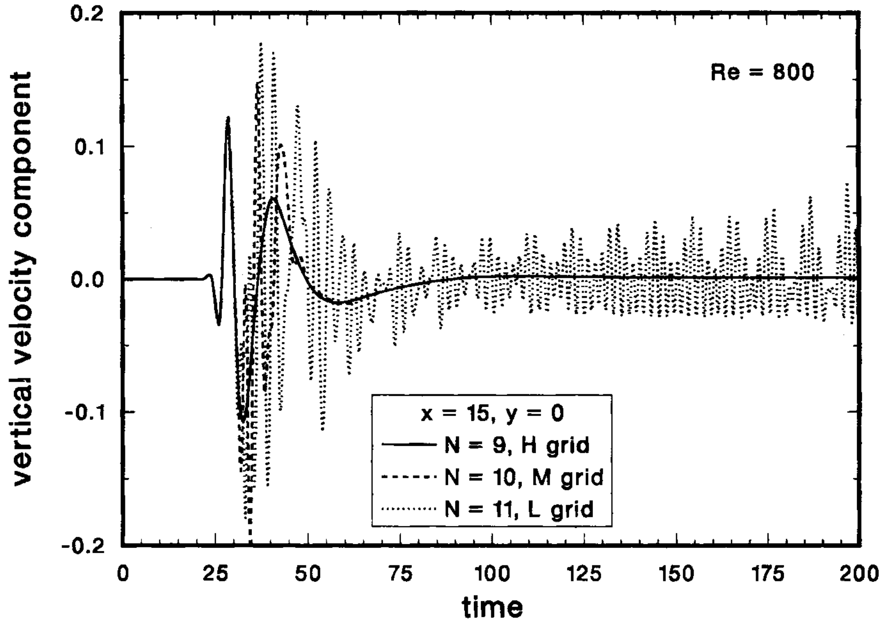

Figure 18. Velocity histories for cases L11, M10 and H09

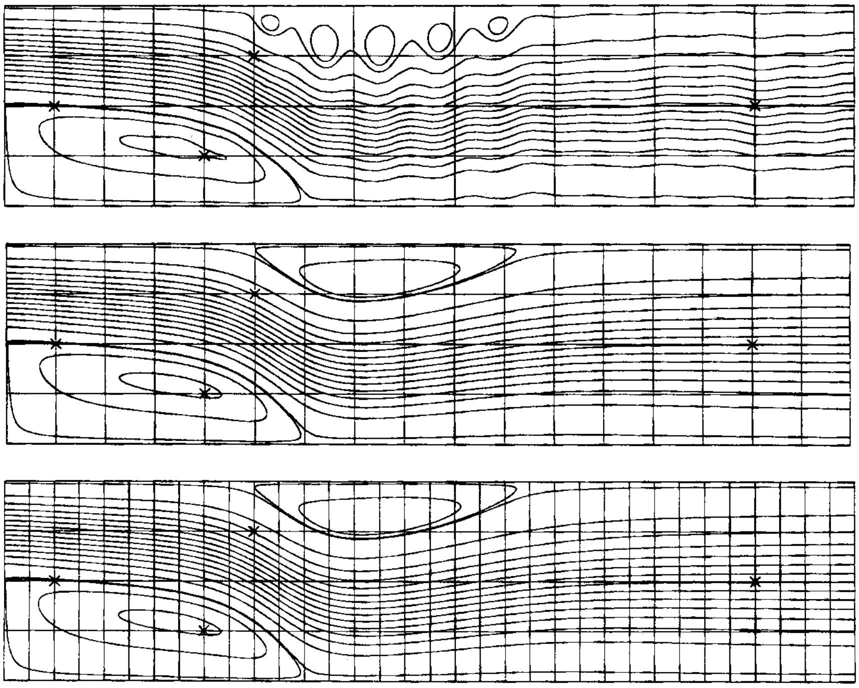

Figure 19. Streamlines at $t=200$: top, case L11; middle, case M10; bottom, case H09 (vertical scale expanded 4:1 for viewing ease)

Table VI. Comparison of present results (extrapolated to $t=\infty$) with Gartling[3]

Quantity	Present study	Gartling[3]
Lower eddy reattachment x location	6·10	6·10
Upper eddy separation x location	4·86	4·85
Upper eddy reattachment x location	10·49	10·48
Stream function at lower eddy centre	−0·0342	−0·0342
Stream function at upper eddy centre	0·5065	0·5064

becomes less stable, with temporally decaying oscillations, and ultimately unstable, at which point it exhibits bounded chaotic behaviour. Further decreases in resolution cause numerical errors to terminate the numerical solution. This trend is observed to hold for resolution changes resulting either from finer subdivision of the computational domain in the streamwise direction or from increases in the element order. Results reported elsewhere[30] for simulations with $Re=500$ and $Re=800$ for the same geometry as KKO show a similar dependence of temporal behaviour on streamwise resolution. Based on these results, the corrct temporal behaviour of flow over a backward-facing step at $Re=800$ seems to be evolution to a stable, asymptotically steady flow by means of a monotonic decay of the transient. This concluison is in disagreement with KKO, where resolution in the streamwise direction appears to be marginal, as discussed above. Note in passing that the appearance of unsteady chaotic flow at low streamwise resolution does not seem to be caused by an instability arising from a violation of the Courant limitation on the time step. To the contrary, since the time step is the same fixed value for all simulations, cases with higher resolution, which yield asymptotically steady behaviour, are actually computed at higher Courant numbers than cases with lower resolution since the nodes are closer together in the cases with higher resolution.

A rigorous explanation for the resolution dependence of the temporal behaviour of numerical solutions determined using spectral element methods has yet to be developed. A tentative mechanism by which inadequate resolution can alter the temporal behaviour of numerical solutions obtained using spectral element methods is as follows. In a spectral element method, inadequate spatial resolution will effectively force high-order polynomials to be fit through spatial variations that are too rapid to be represented accurately. This can produce a non-physical spatial variation (i.e. wiggles) in the underresolved direction. If the wiggles are convected in the underresolved direction, they can induce additional transient spatial variations in the underresolved direction. The polynomial representation continually attempts to follow these transient spatial variations but is unable to do so, and unsteady behaviour results.

Examination of the divergence of the velocity field, $\nabla\cdot\mathbf{u}$, provides some evidence that a mechanism similar to the above is occurring. In the NEKTON post-processor, the divergence is calculated by using the nodal values of the velocity components in conjunction with the analytical derivatives of the polynomial basis functions.[28] Since this approximation to the divergence operator is different from the means by which the NEKTON Uzawa solver enforces a discretely divergence-free velocity field, examination of the divergence during post-processing provides useful diagnostic information about the quality of the numerical solution. In fact, it is this very diagnostic which guided the mesh refinement efforts discussed earlier. Figure 20 shows post-processed divergence contours for the steady and chaotic cases shown in the previous figure. Whenever unsteady chaotic flow is observed, the divergence, calculated as indicated above, is found to be order-unity at *many* locations in the domain, which indicates that the velocity field is not sufficiently well resolved. Nevertheless, even for elements within which the divergence is large,

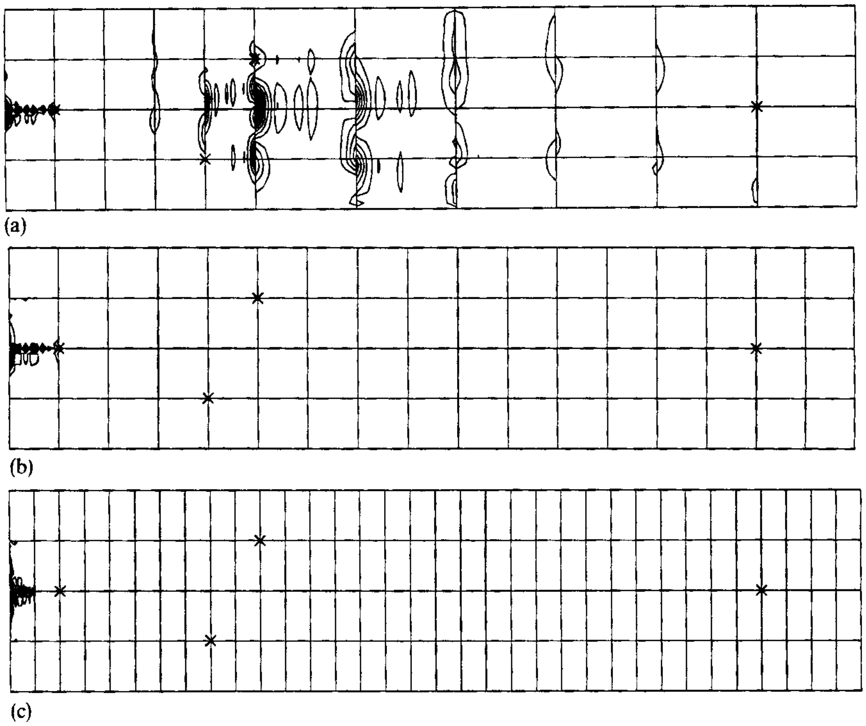

Figure 20. Divergence contours (0·04 between levels) at $t=200$: (a) case L11; (b) case M10; (c), case H09 (vertical scale expanded 4:1 for viewing ease)

the condition of zero net flow out of the element, as required by incompressibility, is well satisfied. Wherever the divergence is appreciably non-zero, it typically exhibits a strong sinusoidal variation in the streamwise direction, indicating that the streamwise direction is underresolved. In all cases with asymptotically steady flow, however, the divergence is close to zero throughout the domain except near the expansion corner, where the flow is weakly singular (the pressure is negatively infinite and the vorticity is multivalued). Since any element basis function not incorporating these features is inherently incapable of representing accurately the resultant steep gradients in this region, a high degree of mesh refinement is required near the corner to minimize the extent of the region within which the flow is poorly represented, namely the elements adjacent to the corner and perhaps their nearest neighbours. On a spectral element mesh, the solution within these elements typically exhibits wiggles and non-zero divergence, as shown in Figure 21. If the spectral element mesh has large elements (a coarse mesh), the region within which the flow is poorly represented can extend significantly into the domain.

Conclusions. Several observations can be made based on the above results. First, inadequate spatial resolution can produce wiggles in spectral element (and other) types of representations of smooth fields. This can occur in a steady fashion near singularities resulting from discontinuities (at some order) in boundary conditions or transiently due to the transient appearance of gradients. Second, inadequate spatial resolution can alter the temporal behaviour of numerical solutions determined by spectral element methods. Third, transient solvers may require more highly refined meshes compared to those required by steady solvers since appreciable gradients may arise transiently in regions where the steady solution has small gradients. Fourth, monitoring the divergence within elements (calculated as indicated above) can indicate regions of

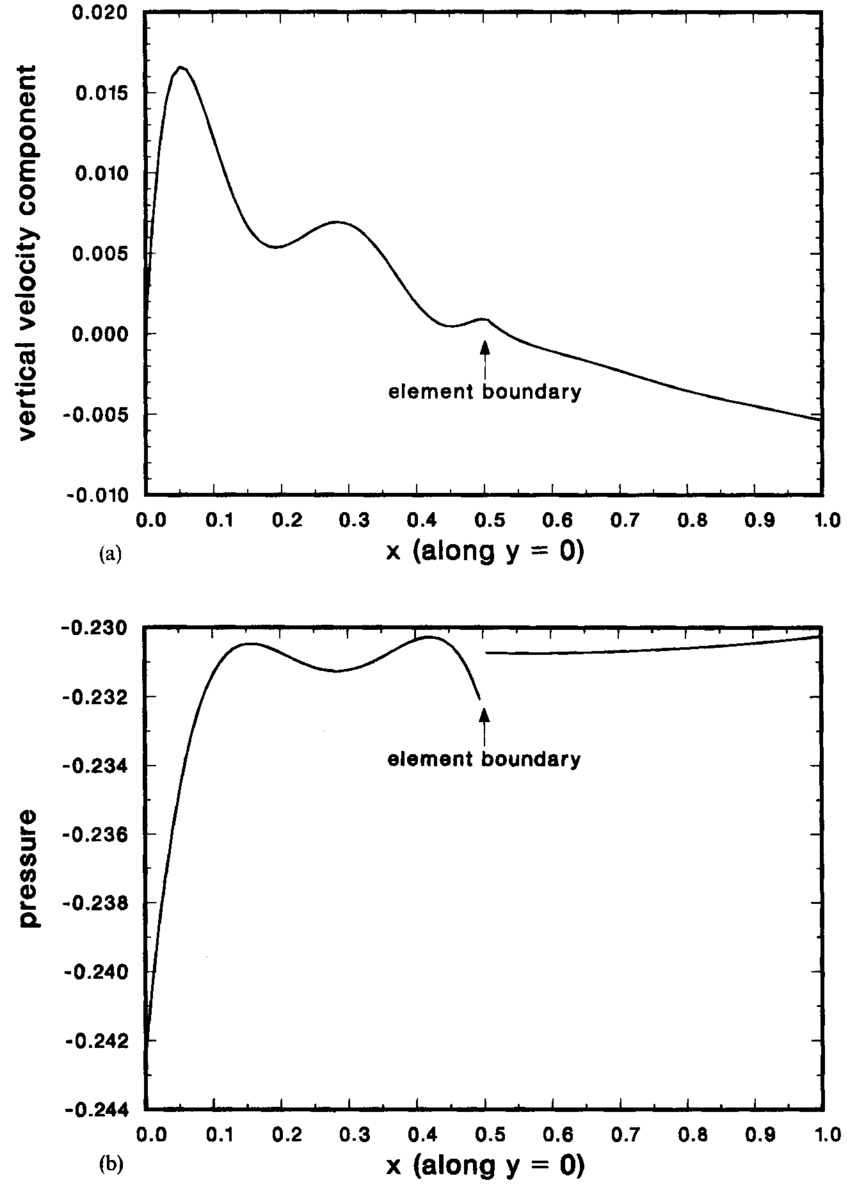

Figure 21. Spatial variations of vertical velocity component (top) and pressure (bottom) near the expansion corner (a weak singularity) for case H07: wiggles result from inadequate spatial resolution

inadequate resolution. This fact may prove useful in developing mesh-refinement strategies to ensure adequate spatial resolution for spectral element methods.

3. DISCUSSION

The principal purpose of this section is to mention a few more studies that were performed at $Re = 800$ via time-marching methods to show, in part, that KKO are actually not alone in

Table VII. 4-node/9-node comparison

	4-node element		9-node element (Gartling)		
	$21 \times 401 =$ 8421 nodes (% error)	$41 \times 801 =$ 32 841 nodes (% error)	$21 \times 201 =$ 8421 nodes (% error)	$41 \times 801 =$ 32 841 nodes	$81 \times 1601 =$ 129 681 nodes
Lower eddy length	5·59 (8·4)	5·95 (2·5)	6·07 (0·49)	6·09	6·10
Upper eddy separation	4·35 (10·3)	4·70 (3·1)	4·83 (0·41)	4·85	4·85
Upper eddy reattachment	10·28 (1·9)	10·43 (0·48)	10·47 (0·10)	10·48	10·48

believing that the solution is not steady. More often than not, however, steady solutions were obtained, leading one to become suspicious of more than just the spectral element method.

We begin by showing some steady results obtained at LLNL[31] using the 4-node bilinear finite element (with piecewise-constant pressure) and the time-marching scheme described in Reference 32—basically forward Euler. Table VII shows that (i) this element is essentially second-order-accurate and (ii) many more 'low-order' elements are needed to obtain the accuracy available from the 'high-order' (9-node biquadratic) element—a 'crude' (and hopefully pessimistic) estimate yields the need for a 100 × 1800 mesh of 18 000 4-node elements to attain just the accuracy of this 9-node element on the 10 × 200 mesh (2000 elements)—not too different from the fine mesh finite difference simulation of Section 2.3 (which also shows similar errors as the 2000 element mesh of 9-node elements). Note that a mesh of N 9-node elements has the same number of velocity nodes as a $4N$ 4-node mesh; and, each node is much more 'accurate'.

The rest of the additional results come from a very recent special session of the ASME,[33] in which we mention only those 7 (of 12) contributions that were performed via time integration. These papers resulted from a follow-on to the original fluid mechanics benchmark problem[3] in which a simple heat transfer problem was appended to the original problem. (It is an uncoupled problem, so that the hard part can be done first, and the simpler advection–diffusion calculation second—unless the first finds no steady state.) A very brief summary of the four simulations that reached a steady solution will be presented first, followed by the three that did not.

(1) Tatsumi *et al.*,[34] a second-order explicit Runge–Kutta method was applied to the semi-discrete (control volume method) equations. Centred second-order spatial differencing was used except for advection, which employed the QUICK method of upwinding.

(2) Pepper *et al.*[35] used the forward Euler method to integrate the semi-discrete equations that were obtained via the FEM using the 4-node (bilinear) element for both velocity and pressure. The usually unstable equal-order method was stabilized (and pressure modes thus precluded) via the 'inconsistent' pressure Poisson equation (see Reference 36).

(3) Schaub and Baker,[37] the stream-function–vorticity version of the equations was discretized using bilinear (4-node) finite elements and the resulting semi-discrete equations were marched in time via either backward Euler or trapezoid rule. (They did not state which they used).

(4) Dyne and Heinrich[38] used bilinear finite elements on the 'penalty' version of the Navier–Stokes equations (with Petrov–Galerkin weighting rather than the usual Galerkin weighting) and marched them to steady state with a semi-implicit method (explicit for advection)—but no further details were given.

We now summarize the three papers from this conference that did *not* find the steady-state solution.

(5) Runchal[39] used the finite volume discretization method with a second-order TVD scheme for advection to generate the semi-discrete equations which were then marched forward via the SIMPLE method. The oscillatory solution was 'justified' by noting that a steady (but wrong, owing to numerical diffusion) solution was obtained if they used the hybrid upwind method rather than the TVD method.
(6) Choudhury[40] used the FLUENT finite volume code, with QUICK for advection and co-located velocity and pressure variables. The SIMPLEC algorithm was used for velocity-pressure coupling but details of the time-marching method were not reported—only that an oscillatory solution was the result, *à la* KKO whom they reference for 'verification.'
(7) Chakrabarti and Subbiah[41] used Fluent's NEKTON code (spectral element) with a splitting (fractional step) marching scheme to obtain, like KKO, 'some unsteady behaviour suggesting that the flow is not truly steady at Reynolds number of 800.'

Returning now to the KKO paper, whose results we have demonstrated to be underresolved, we note their additional statements, 'At Reynolds number $Re=700$ the flow has already undergone its first bifurcation,' and 'Our results suggest that the transition process starts at approximately $Re \cong 700$ with fluctuations becoming increasingly larger as Re approaches 1000.' Their results, as well as those of Sethian and Ghoniem,[8] Runchal,[39] Choudhury[40] and Chakrabarti and Subbiah,[41] show that much care is required not to fall into the trap of numerically-generated transient fluid dynamics, *à la* 'The Dynamics of Numerics', see e.g. Reference 42.

As a final point relating to the extra care needed by spectral (and spectral element) method practitioners, we quote from a recent paper by Schumack *et al.*,[43] who solved one of the simplest of all problems—the steady Stokes equations–10 different ways using spectral methods: 'The presence of corner singularities destroys the accuracy of spectral methods.' Unfortunately, there are many 'real' fluid mechanical simulations that do not generate 'sufficiently smooth' solutions; perhaps 'rough' solutions are more appropriately simulated using rough (low-order) numerical methods, on grids that 'adapt' to singularities via mesh refinement.

4. CONCLUSIONS

In spite of several opinions to the contrary, the $t \to \infty$ solution of the incompressible Navier–Stokes equations past a backward-facing step at $Re=800$ is steady and stable.

But there are other important conclusions from this long and expensive study that are worth mentioning—because we believe that some generalizing is appropriate (i.e. it is likely that there are other rogue solutions in the published literature, with perhaps more to come):

(1) Journals *and* their referees must remain vigilant to demonstrations of accuracy and convergence, especially when new fluid mechanical phenomena are being proposed or explained.
(2) CFD is not easy, even today; much care is required.
(3) While not professing to be benchmark zealots, we believe that it is worthwhile to generate both a small set of them (benchmarks) and to require 'numerical' papers to show agreement with at least some subset of them, especially if the paper has uncovered something new and/or different.
(4) The circumstances that 'caused' the study are unfortunate, but probably useful in the long run.

ACKNOWLEDGEMENTS

The work of P. M. Gresho was performed under the auspices of the U.S. Department of Energy by the Lawrence Livermore National Laboratory under contract No. W-7405-Eng-48 and that of D. K. Gartling and J. R. Torczynski was performed at Sandia National Laboratories, supported by the U.S. Department of Energy under contract DE-AC04-76DP00789.

REFERENCES

1. P. M. Gresho, 'A summary report on the 14 July minisymposium on outflow BCs for incompressible flow', in *Proceedings, 4th Int. Symp. on Computational Fluid Dynamics*, University of California at Davis, 9–12 September 1991, p. 436.
2. R. Sani and P. M. Gresho, 'Summary of two minisymposia on outflow boundary conditions for incompressible flow', *Int. j. numer. methods fluids* (in press).
3. D. K. Gartling, 'A test problem for outflow boundary conditions—flow over a backward-facing step', *Int. j. numer. methods fluids*, **11**, 953–967 (1990).
4. P. M. Gresho, 'Some current CFD issues relevant to the incompressible Navier–Stokes equations', *Comput. Methods Appl. Mech. Eng.*, **87**, 201–252 (1991).
5. L. Kaiktsis, G. E. Karniadakis and S. Orszag, 'Onset of three-dimensionality, equilibria, and early transition in flow over a backward facing step', *J. Fluid Mech.*, **231**, 501–528 (1991).
6. G. A. Osswald, K. N. Ghia and U. Ghia, 'Study of incompressible flow using an implicit time-dependent technique', *Proc. 6th Comput. Fluid Dyn. Conf.*, AIAA, New York, 1983, pp. 686–696.
7. J. Kim and P. Moin, 'Application of a fractional step method to the incompressible Navier–Stokes equations', *J. Comput. Phys.*, **59**, 308 (1985).
8. J. A. Sethian and A. F. Ghoniem, 'Validation study of vortex methods', *J. Comput. Phys.*, **74**, 283 (1988).
9. A. F. Ghoniem and J. A. Sethian, 'Effect of Reynolds number on the structure of recirculating flow', *AIAA J.*, **25**, 1, 168 (1987).
10. D. K. Gartling, 'NACHOS II—A finite element code for incompressible flow problems', *Sandia National Laboratories Report, SAND86-1816 and SAND86-1817*, Albuquerque, NM, 1987.
11. P. M. Gresho, R. L. Lee and R. L. Sani, 'On the time dependent solution of the incompressible Navier–Stokes equations in two and three dimensions', in *Recent Advances in Numerical Methods in Fluids, Vol. 1*, Pineridge Press, Swansea, 1980, pp. 27–81.
12. K. H. Winters, *ENTWIFE User Manual (Release 1), Harwell Report AERE-R 11577*, 1985.
13. P. M. Gresho, R. L. Sani and M. S. Engelman, *Incompressible Flow and the Finite Element Method*, (in preparation).
14. W. C. Rheinboldt, *Numerical Analysis of Parameterised Nonlinear Equations*, Wiley-Interscience, New York, 1986.
15. M. W. Hirsch and S. Smale, *Differential Equations, Dynamical Systems and Linear Algebra*, Academic Press, New York, 1974.
16. K. A. Cliffe and A. Spence, 'On a generalized eigenvalue problem arising from discretisations of the Navier–Stokes equations', (in preparation).
17. K. A. Cliffe, T. J. Garratt and A. Spence, 'Iterative methods for the detection of Hopf bifurcations in finite element discretisations of incompressible flow problems', *SIAM J. Sci. Comput.* (submitted).
18. D. Malkus, 'Eigenproblems associated with the discrete LBB condition for incompressible finite elements', *Int. J. Eng. Sci.*, **19**, 1299 (1981).
19. A. Jennings and G. W. Stewart, 'Simultaneous iteration for the partial eigensolution of real matrices', *J. Inst. Math. Appl.*, **15**, 351–362 (1975).
20. R. Schreiber and H. B. Keller, 'Driven cavity flows by efficient numerical techniques', *J. Comput. Phys.*, **49**, 310 (1983).
21. J. Linden, 'A multigrid method for solving the biharmonic equation on rectangular domains', *Arbeitspapiere der GMD No. 143*, Gesellschaft für Mathematik und Datenverarbeitung, St. Augustin, 1985.
22. P. M. Gresho, 'Some interesting issues in incompressible fluid dynamics, both in the continuum and in numerical simulation', *Adv. Appl. Mech.*, **28**, 45 (1992).
23. J. W. Goodrich and W. Y. Soh, 'Time-dependent viscous incompressible Navier–Stokes equations: the finite difference Galerkin formulation and stream function algorithms', *J. Comput. Phys.*, **84**, 207 (1989).
24. J. W. Goodrich, 'An unsteady time asymptotic flow in the square driven cavity', in K. Gustafson and W. Wyss (eds), *Proc. IMACS 1st Int. Conf. on Comput. Phys.*, University of Colorado at Boulder, 1990; *NASA TM 103141*, 1990.
25. J. W. Goodrich, 'An efficient and robust algorithm for two dimensional time dependent incompressible Navier–Stokes equations: high Reynolds number flows', in C. Taylor, J. H. Chin and G. M. Homsy (eds), *Numerical Methods in Laminar and Turbulent Flow, Vol. VII: Proc. 7th Int. Conf. Stanford*, 15–19 July, 1991; *NASA TM 104424*, 1991.
26. J. W. Goodrich (in preparation).
27. J. W. Goodrich and T. Hagstrom (in preparation).
28. *NEKTON User's Guide*, Version 2.7, Nektonics Inc., Cambridge, MA, 1991.
29. A. T. Patera, 'A spectral element method for fluid dynamics: laminar flow in a channel expansion', *J. Comput. Phys.*, **54**, 468–488 (1984).

30. J. R. Torczynski, 'Simulations of two-dimensional transient flow over a backward-facing step using a spectral-element method', in R. A. Bajura (ed.), *Fluids Engineering 1992 Abstracts,* FED-Vol. 133, American Society of Mechanical Engineers, New York, 1992, pp. 185–186.
31. R. McCallen, 'Large-eddy simulation of turbulent flow using the finite element method', *Ph.D. Thesis,* U. C. Davis, Department of Mechanical Engineering, (1993).
32. P. M. Gresho, S. Chan, C. Upson and R. Lee, 'A modified finite element method for solving the time-dependent, incompressible Navier–Stokes equations, Part 1 (Theory)', *Int. j. numer. methods fluids,* **4,** 557 (1984); Part 2 (Applications), ibid **4,** 619 (1984).
33. B. Blackwell and D. W. Pepper (eds), 'Benchmark problem for heat transfer codes', *Proc. Winter Annual Meeting of the ASME,* Anaheim, HTD-Vol. 222, CA, 8–13 November, 1992.
34. K. Tatsumi, W. Usry and J. Humphrey, 'Numerical calculations of two dimensional laminar flow and heat transfer for a backward facing step', in B. Blackwell and D. W. Pepper (eds), *Proc. Winter Annual Meeting of the ASME,* Anaheim, 1992, p. 1.
35. D. W. Pepper, K. Burton, F. Brueckner and B. Blackwell, 'Numerical simulation of laminar flow and heat transfer over a backward facing step, in B. Blackwell and D. W. Pepper (eds), *Proc. Winter Annual Meeting of the ASME,* Anaheim, 1992, p. 21.
36. P. M. Gresho, 'An analysis of the velocity correction method of M. Kawahara *et al.*', *Bull. Faculty Sci. Eng.* (Chuo Univ.), **30,** 45 (1987).
37. E. G. Schaub and A. J. Baker, 'Step-wall diffuser benchmark prediction/boundary condition implementation in an AKCESS', in B. Blackwell and D. W. Pepper (eds), *Proc. Winter Annual Meeting of the ASME,* Anaheim, 1992, p. 45.
38. B. R. Dyne and J. D. Heinrich, 'Flow over a backward facing step: a benchmark problem for laminar flow with heat transfer', in B. Blackwell and D. W. Pepper (eds), *Proc. Winter Annual Meeting of the ASME,* Anaheim, 1992, p. 73.
39. A. K. Runchal, 'ANSWER: A benchmark study for backward facing step', in B. Blackwell and D. W. Pepper (eds), *Proc. Winter Annual Meeting of the ASME,* Anaheim, 1992, p. 13.
40. D. Choudhury, 'A finite-volume CFD code', in B. Blackwell and D. W. Pepper (eds), *Proc. Winter Annual Meeting of the ASME,* Anaheim, 1992, p. 53.
41. M. Chakrabarti and S. Subbiah, 'A spectral-element solution to the backward-facing step problem using NEKTON', in B. Blackwell and D. W. Pepper (eds), *Proc. Winter Annual Meeting of the ASME,* Anaheim, 1992, p. 59.
42. A. C. Yee, P. Sweby and D. F. Griffiths, 'Dynamical approach study of steady-state numerical solutions of nonlinear differential Equations. 1. The dynamics of time discretization and its implications for algorithm development in computational fluid dynamics', *J. Comput. Phys.,* **97,** 249 (1991).
43. M. Schumack, W. Schultz and J. Boyd, 'Spectral method solution of the Stokes equations on nonstaggered grids', *J. Comput. Phys.,* **94,** 30 (1991).